

# High-fidelity controlled- $\sigma^z$ gate for resonator-based superconducting quantum computers

Joydip Ghosh,<sup>1,\*</sup> Andrei Galiutdinov,<sup>1,2</sup> Zhongyuan Zhou,<sup>1</sup> Alexander N. Korotkov,<sup>2</sup>  
John M. Martinis,<sup>3</sup> and Michael R. Geller<sup>1,†</sup>

<sup>1</sup>*Department of Physics and Astronomy, University of Georgia, Athens, Georgia 30602, USA*

<sup>2</sup>*Department of Electrical Engineering, University of California, Riverside, California 92521, USA*

<sup>3</sup>*Department of Physics, University of California, Santa Barbara, California 93106, USA*

(Received 11 June 2012; revised manuscript received 5 January 2013; published 8 February 2013)

A possible building block for a scalable quantum computer has recently been demonstrated [Mariantoni *et al.*, *Science* **334**, 61 (2011)]. This architecture consists of superconducting qubits capacitively coupled both to individual memory resonators as well as a common bus. In this work we study a natural primitive entangling gate for this and related resonator-based architectures, which consists of a controlled- $\sigma^z$  (CZ) operation between a qubit and the bus. The CZ gate is implemented with the aid of the noncomputational qubit  $|2\rangle$  state [Strauch *et al.*, *Phys. Rev. Lett.* **91**, 167005 (2003)]. Assuming phase or transmon qubits with 300 MHz anharmonicity, we show that by using only low frequency qubit-bias control it is possible to implement the qubit-bus CZ gate with 99.9% (99.99%) fidelity in about 17 ns (23 ns) with a realistic two-parameter pulse profile, plus two auxiliary  $z$  rotations. The fidelity measure we refer to here is a state-averaged intrinsic process fidelity, which does not include any effects of noise or decoherence. These results apply to a multiqubit device that includes strongly coupled memory resonators. We investigate the performance of the qubit-bus CZ gate as a function of qubit anharmonicity, identify the dominant intrinsic error mechanism and derive an associated fidelity estimator, quantify the pulse shape sensitivity and precision requirements, simulate qubit-qubit CZ gates that are mediated by the bus resonator, and also attempt a global optimization of system parameters including resonator frequencies and couplings. Our results are relevant for a wide range of superconducting hardware designs that incorporate resonators and suggest that it should be possible to demonstrate a 99.9% CZ gate with existing transmon qubits, which would constitute an important step towards the development of an error-corrected superconducting quantum computer.

DOI: [10.1103/PhysRevA.87.022309](https://doi.org/10.1103/PhysRevA.87.022309)

PACS number(s): 03.67.Lx, 85.25.Cp

## I. QUANTUM VON NEUMANN ARCHITECTURE

Reaching the fidelity threshold for fault-tolerant quantum computation with superconducting electrical circuits [1–3] will probably require improvement in three areas: qubit coherence, readout, and qubit-qubit coupling tunability. Fortunately, the coherence times of superconducting transmon qubits [4,5] have increased dramatically, exceeding  $10\ \mu\text{s}$  in the three-dimensional version [6,7]. Fast, threshold-fidelity nondestructive measurement has not yet been demonstrated, but is being actively pursued [8–12]. Some method for turning off the interaction between device elements—beyond simple frequency detuning—is also desirable for high-fidelity operations. A variety of tunable coupling circuits have been demonstrated [13–19], but these considerably increase the complexity of the hardware and it is not clear whether they will be practical for large-scale implementation. The coupling can also be controlled by the application of microwave pulses [20–32].

An alternative approach has been introduced by Mariantoni *et al.* [33] and theoretically analyzed in Ref. [34]. In this *quantum von Neumann* (QVN) architecture, superconducting qubits are capacitively coupled both to individual memory resonators as well as a common bus, as illustrated in Fig. 1. The crossed boxes in Fig. 1 represent the phase qubits [35] employed by Mariantoni *et al.* [33], however, other qubit designs such as the transmon may be used here as well. The key feature of this architecture is that information (data) is stored in memory resonators that are isolated by *two* detuned coupling

steps from the bus. Qubits are used to transfer information to and from the bus or entangle with it, and to implement single-qubit operations, but are otherwise kept in their ground states. No more than one qubit (attached to the same bus) is to be occupied at any time. Such an approach significantly improves the effective on-off ratio without introducing the added complexity of nonlinear tunable coupling circuitry. The spectral crowding problem of the usual qubit-bus architecture is greatly reduced because the four-step coupling between memory resonators is negligible. And an added benefit of the QVN approach is that the longer coherence times of the memory elements reduce the overall decoherence rate of the device. (In Ref. [34], the architecture we consider is referred to as the resonator-zero-qubit architecture, but here we will follow the QVN terminology of [33].)

The QVN architecture of Mariantoni *et al.* [33] is not, by itself, capable of large-scale, fault-tolerant quantum computation, nor is it known how multiple QVN devices might be integrated into a scalable design. The problem of designing scalable, fault-tolerant architectures for superconducting qubits is of great interest and importance [36,37], but is still in its infancy. We expect the gate design approach discussed here to be applicable to future architecture designs incorporating qubits coupled to resonators, and perhaps beyond.

Along with high-fidelity single-qubit rotations [38,39], quantum computing with the QVN processor requires two additional types of operations. The first is state transfer between the different physical components, which has to be performed frequently during a computation. The simplest case of state transfer is between a qubit and its associated memory (or the reverse). This case is investigated in Ref. [34],

\*joydip.ghosh@gmail.com

†mgeller@uga.edu

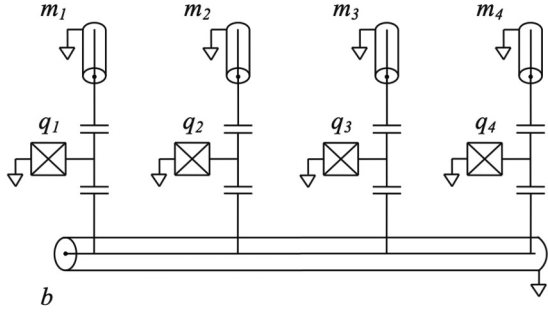


FIG. 1. Layout of the four-qubit QVN processor. The  $q_i$  represent superconducting qubits capacitively coupled to memory resonators  $m_i$  as well as a resonator bus  $b$ .

where two important observations are made: First, in contrast with the usual SWAP or ISWAP operations, which must be able to simultaneously transfer quantum information in two directions, only unidirectional state transfers are required in the QVN system. This is because adjacent qubits and resonators are—by agreement—never simultaneously populated. Second, the phase of a transferred  $|1\rangle$  state is immaterial, as it can always be adjusted by future qubit  $z$  rotations [40,41]. These two simplifications allow the resulting state transfer operation, called a MOVE gate, to be carried out with extremely high intrinsic fidelity—perfectly for a truncated model—with a simple four-parameter pulse profile. By intrinsic fidelity we mean the process fidelity (defined below) in the absence of noise or decoherence. The need for four control parameters immediately follows from the requirement that after a MOVE gate, the probability amplitudes must vanish on two device components, the component ( $q$  or  $m$ ) the state is leaving, and the bus  $b$ . Each zero imposes two real parameters, and no other probability amplitudes acquire weight (in the truncated model). Fixing the phase of the MOVE gate, if desired, requires one additional control parameter in the form of a local  $z$  rotational angle.

State transfer between a qubit and the bus (or the reverse) can be analyzed in the same way, although in this case more pulse-shape parameters are required. In an  $n$ -qubit QVN processor (consisting of  $n$  qubits,  $n$  memory resonators, and the bus), zero-amplitude conditions must be enforced on the additional  $n - 1$  qubits, leading to a total of  $2(n + 1)$  pulse parameters, plus one  $z$  rotation angle. This makes quasixact state transfer to and from the bus a considerably more challenging operation. Simpler three-parameter approximate transfers, however, can still be implemented with very high fidelity, even when the coupling is strong (see below).

Quantum computing with the QVN system also requires a universal SU(4) entangling gate, the most natural being a controlled- $\sigma^z$  (CZ) operation between a qubit and the bus. The CZ gate investigated here makes essential use of the noncomputational qubit  $|2\rangle$  state and was first proposed by Strauch and coworkers [42]. The Strauch gate has been investigated by many authors and has been demonstrated in several systems [43–48].

The present paper extends previous work by considering device parameters and pulse shapes appropriate for the QVN system, and by optimizing the CZ fidelity in a multiqubit device. We are especially interested in whether the absence of

an active tunable coupler results in any significant limitation on the obtainable fidelity, given a reasonable amount of qubit coherence, and whether very high intrinsic fidelities can be reached with a simple and experimentally realistic (filtered rectangular) pulse shape. We also study how the gate performance rapidly improves with increasing qubit anharmonicity, show that the dominant intrinsic error is caused by a nonadiabatic excitation of the bus  $|2\rangle$  state that occurs during the switching of the qubit frequency, derive a fidelity estimator based on that mechanism, analyze pulse shape errors, and simulate qubit-qubit CZ gates mediated by the bus. Finally, we address the interesting problem of *system optimization*, by using gate and idling error estimates to deduce optimal values of resonator frequencies and couplings.

## II. SUMMARY OF RESULTS

We find that very high intrinsic fidelities—in the range of 99.9% to 99.99% and with corresponding total gate times in the range of 17–23 ns—can indeed be obtained with a four-parameter gate. Two control parameters are pulse-shape parameters and two are auxiliary local  $z$  rotation angles. We emphasize that only low-frequency pulses are required, and that the number of control parameters does not depend on the number of qubits in the QVN device. The results quoted above assume four phase or transmon qubits with 300 MHz anharmonicity; other values of anharmonicity are considered below. The CZ gate referred to here is between qubit  $q_1$  and the bus (see Fig. 1), not between a pair of qubits as is usually considered.

The two-parameter low frequency pulse profile we use throughout this work is

$$\epsilon(t) = \omega_{\text{off}} + \frac{\omega_{\text{on}} - \omega_{\text{off}}}{2} \left[ \text{Erf} \left( \frac{t - \frac{1}{2}t_{\text{ramp}}}{\sqrt{2}\sigma} \right) - \text{Erf} \left( \frac{t - t_{\text{gate}} + \frac{1}{2}t_{\text{ramp}}}{\sqrt{2}\sigma} \right) \right], \quad (1)$$

an example of which is shown in Fig. 2. Here  $\epsilon$  is the qubit frequency,  $\omega_{\text{off}}$  and  $\omega_{\text{on}}$  are the frequencies off and near resonance (with the bus), and the pulse switching time is determined by  $\sigma$ , the standard deviation of the Gaussians inside (1). The value of  $t_{\text{ramp}}$  determines how the pulse is truncated at  $t = 0$  and  $t_{\text{gate}}$  as explained in Sec. III F; throughout this work we assume that

$$t_{\text{ramp}} = 4\sqrt{2}\sigma. \quad (2)$$

The relation (2) allows the switching time to be alternatively characterized by  $t_{\text{ramp}}$ , which, as Fig. 2 illustrates, is a measure of the width of the ramps. The variable  $t_{\text{gate}}$  is the total execution time of the gate excluding  $z$  rotations. The two control parameters,  $\omega_{\text{on}}$  and

$$t_{\text{on}} \equiv t_{\text{gate}} - t_{\text{ramp}}, \quad (3)$$

are determined by the numerical optimization procedure described in Sec. III G. From (3) we infer that  $t_{\text{on}}$  is the time interval between the midpoints of the ramps, or the full width at half maximum (FWHM) of the pulse. We note that the optimal

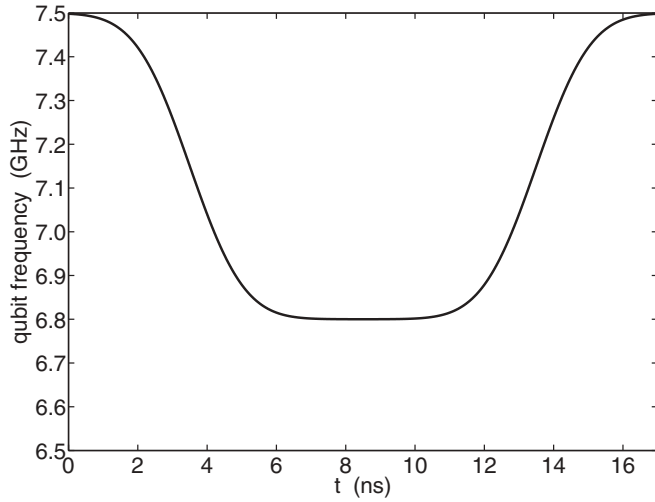


FIG. 2. Two-parameter CZ pulse profile (1) for the case of  $\omega_{\text{on}}/2\pi = 6.8$  GHz,  $\omega_{\text{off}}/2\pi = 7.5$  GHz,  $t_{\text{ramp}} = 7$  ns,  $\sigma = 1.24$  ns, and  $t_{\text{on}} = 10$  ns. The total gate time excluding auxiliary  $z$  rotations is  $t_{\text{gate}} = 17$  ns. The example shown is representative of a 99.9% fidelity gate for a qubit with 300 MHz anharmonicity.

values of  $t_{\text{on}}$  are somewhat longer than the value,

$$t_{\text{on}}^{\text{sudden}} \equiv \frac{\pi}{\sqrt{2}g_b}, \quad (4)$$

that applies in the sudden,  $\sigma \rightarrow 0$  limit. In addition to  $\omega_{\text{on}}$  and  $t_{\text{on}}$ , two auxiliary local  $z$  rotations—on the qubit and resonator—are used to implement the CZ gate. As we explain below, adjusting the two control parameters  $\omega_{\text{on}}$  and  $t_{\text{on}}$  zeros the population left in the noncomputational qubit  $|2\rangle$  state after the gate and (along with the auxiliary  $z$  rotations) sets the controlled phase equal to  $-1$ . The pulse shape (1) describes a rectangular current or voltage pulse sent to the qubit frequency bias through a Gaussian filter of width  $\sigma$ , and is believed to be an accurate (although not exact) representation of the actual profile seen by the qubits in Ref. [33].

Our main results are given in Table I. Here  $\eta$  is the qubit anharmonicity. The 200-MHz results apply to the phase qubits of Ref. [33], while the larger anharmonicities might be relevant for future implementations with transmons. The bus couplings  $g_b$  are determined by the “ $g$  optimization” procedure described

in Sec. V, which leads to the simple formula,

$$\frac{g_b}{\eta} = 0.15, \quad (5)$$

for the (approximately) optimal bus coupling. Let  $\text{QVN}_n$  refer to a quantum von Neumann processor with  $n$  qubits coupled to  $n$  memory resonators and a bus; the Hamiltonian for such a device is discussed in Sec. III A. As indicated in Table I, the memory resonators are always strongly coupled to allow for fast (less than 5 ns) MOVE operations in and out of memory. CZ fidelities well above 99.99% are also obtainable (see Sec. III J). Table I shows that the time required for a qubit-bus CZ gate with fixed intrinsic fidelity is inversely proportional to the qubit anharmonicity, namely,

$$t_{\text{gate}}^{(99.9\%)} \approx \frac{5.2}{\eta/2\pi} \quad \text{and} \quad t_{\text{gate}}^{(99.99\%)} \approx \frac{6.7}{\eta/2\pi}. \quad (6)$$

These expressions indicate that CZ gates with very high intrinsic fidelity can be implemented in about 20 ns with existing superconducting qubits, a conclusion which applies not only to  $\text{QVN}_n$  but also to a wide range of similar resonator-based architectures. The intrinsic gate (or process) fidelity  $F_{\text{ave}}$  is the squared overlap of ideal and realized final states, averaged over initial states (see Sec. III E). By *intrinsic* we mean that noise and decoherence are not included in the gate simulation. The fidelity estimate is developed in Sec. III H. The results given in Table I apply specifically to the  $n = 4$  processor, but similar results are expected for other (not too large) values of  $n$ . Two strategies are critical for obtaining this high performance: separating two control parameters in the form of auxiliary local  $z$  rotations, and defining the computational states in terms of *interacting* system eigenfunctions. These strategies were used in Ref. [34] and are discussed in more detail below. The gate fidelities achievable with a transmon-based  $\text{QVN}$  device are in line with that required for fault-tolerant quantum computation with topological stabilizer codes [49–51]. Qubit anharmonicity is an important resource that will help us achieve that goal.

The CZ gate of Table I is between qubit  $q_1$  and the bus in the  $\text{QVN}_4$  device, and begins (typically) with a superposition of qubit-bus eigenstates, with the other qubits and all memory resonators in their ground states. In Sec. IV we also comment on several extensions and variations of this basic qubit-bus CZ gate: To begin with, the same gate but with qubit  $q_4$  (which has a different memory frequency) is considered in Sec. IV A. In Sec. IV B we simulate a CZ gate between two *qubits* in  $\text{QVN}_4$ ,

TABLE I. Optimal state-averaged process fidelity  $F_{\text{ave}}$  for the Strauch CZ gate between qubit  $q_1$  and the bus, in the  $\text{QVN}_4$  processor of Fig. 1. No decoherence or noise is included here. Specifications for 99.9% and 99.99% gates are provided for three values of qubit anharmonicity  $\eta$ . The parameters  $t_{\text{ramp}}$  and  $\sigma$  characterize the pulse switching time, and  $t_{\text{gate}}$  is the total gate time excluding auxiliary  $z$  rotations.  $F_{|11\rangle}$  is the minimum fidelity. Data after vertical line give the nonadiabatic switching error and minimum fidelity estimates; these quantities are defined and discussed in Sec. III H.

$\eta/2\pi$	$g_b/2\pi$	$g_m/2\pi$	$t_{\text{on}}^{\text{sudden}}$	$t_{\text{ramp}}$	$\sigma$	$t_{\text{on}}$	$t_{\text{gate}}$	$F_{\text{ave}}$	$F_{ 11\rangle}$	$ A ^2$	$p_{\text{sw}}$	$F_{ 11\rangle}^{(\text{est})}$
200 MHz	30 MHz	100 MHz	11.8 ns	11 ns	1.94 ns	15.8 ns	26.8 ns	99.901%	99.613%	$2.1 \times 10^{-2}$	$1.5 \times 10^{-3}$	99.692%
				16 ns	2.83 ns	18.3 ns	34.3 ns	99.992%	99.975%	$2.8 \times 10^{-3}$	$2.0 \times 10^{-4}$	99.960%
300 MHz	45 MHz	100 MHz	7.9 ns	7 ns	1.24 ns	9.9 ns	16.9 ns	99.928%	99.714%	$1.7 \times 10^{-2}$	$1.2 \times 10^{-3}$	99.761%
				11 ns	1.94 ns	11.8 ns	22.8 ns	99.995%	99.979%	$9.9 \times 10^{-4}$	$7.2 \times 10^{-5}$	99.986%
400 MHz	60 MHz	100 MHz	5.9 ns	5 ns	0.88 ns	7.0 ns	12.0 ns	99.950%	99.804%	$1.4 \times 10^{-2}$	$1.0 \times 10^{-3}$	99.799%
				7 ns	1.24 ns	7.8 ns	14.8 ns	99.991%	99.966%	$2.1 \times 10^{-3}$	$1.5 \times 10^{-4}$	99.970%

starting in the idling configuration where the qubits are empty and all data is stored in memory. In this case the qubit-bus CZ gate of Table I is supplemented with MOVE gates to effect a CZ between qubits. And in Sec. IV C we discuss the CZ implemented between a pair of *directly* coupled anharmonic qubits, instead of a qubit and resonator. This is the system originally considered by Strauch *et al.* [42].

### III. CZ GATE DESIGN

In this section we discuss the qubit-bus CZ gate design problem.

#### A. QVN model

The QVN<sub>n</sub> processor consists of  $n$  superconducting qubits [1–3] capacitively coupled [42,52,53] to  $n$  memory resonators and to a common bus resonator. Here we assume parameters appropriate either for phase qubits [35] or transmon qubits

[4,5] with tunable transition frequencies. We write the qubit angular frequencies as  $\epsilon_i$ , with  $i = 1, \dots, n$ . These are the only controllable parameters in the QVN Hamiltonian (in contrast with Refs. [20–32] we do not make use of microwave pulses). The memory frequencies are written as  $\omega_{mi}$ , and the bus frequency is  $\omega_b$ . The (bare) frequencies of all resonators are assumed here to be fixed.

Because we are interested in very high fidelities, a realistic model is required. However, we have shown (in unpublished work) that the CZ performance is extremely robust with respect to the model details, so we only report results for a simplified Hamiltonian; the approximations used are discussed below. For the qubit-bus CZ simulations, the Hilbert space is truncated to allow for up to three excitations. The CZ gate naively involves no more than two excitations, so to properly account for leakage we include up to three. Therefore, four-level qubits and resonators (which include the  $|3\rangle$  states) are required in the model. The QVN Hamiltonian is

$$H = \sum_{i=1}^n \left[ \begin{pmatrix} 0 & 0 & 0 & 0 \\ 0 & \epsilon_i & 0 & 0 \\ 0 & 0 & 2\epsilon_i - \eta & 0 \\ 0 & 0 & 0 & 3\epsilon_i - \eta' \end{pmatrix}_{qi} + \begin{pmatrix} 0 & 0 & 0 & 0 \\ 0 & \omega_{mi} & 0 & 0 \\ 0 & 0 & 2\omega_{mi} & 0 \\ 0 & 0 & 0 & 3\omega_{mi} \end{pmatrix}_{mi} + g_m Y_{qi} \otimes Y_{mi} + g_b Y_{qi} \otimes Y_b \right] + \begin{pmatrix} 0 & 0 & 0 & 0 \\ 0 & \omega_b & 0 & 0 \\ 0 & 0 & 2\omega_b & 0 \\ 0 & 0 & 0 & 3\omega_b \end{pmatrix}_b, \quad (7)$$

excluding single-qubit terms for microwave pulses that are not used in this work. Here  $\eta$  and  $\eta'$  are qubit anharmonic detuning frequencies,  $g_m$  and  $g_b$  are the qubit-memory and qubit-bus interaction strengths, and

$$Y \equiv \begin{pmatrix} 0 & -i & 0 & 0 \\ i & 0 & -\sqrt{2}i & 0 \\ 0 & \sqrt{2}i & 0 & -\sqrt{3}i \\ 0 & 0 & \sqrt{3}i & 0 \end{pmatrix}. \quad (8)$$

The matrices in (7) act nontrivially in the spaces indicated by their subscripts, and as the identity otherwise. The matrix  $Y$  results from a harmonic oscillator approximation for the qubit eigenfunctions. Factors of  $\hbar$  are suppressed throughout this paper.

The main approximations leading to (7) are the neglect of the  $\epsilon$  dependence of the interaction strengths  $g_m$  and  $g_b$ , and the neglect of a small direct coupling between the memories and bus [54]. We have verified that including these does not change the main conclusions of this work. The  $\epsilon$  dependence of the anharmonicities  $\eta$  and  $\eta'$ , and small anharmonic corrections to the interaction terms in (7), are also neglected.

The parameter values we use in our simulations are provided in Table II. We assume  $\eta' = 3\eta$ , which is appropriate for cubic anharmonicity. As discussed in Sec. V, the value of the bus coupling  $g_b$  is chosen to give the shortest CZ gate time (for a range of fidelities). The choice of resonator frequencies is also discussed in Sec. V. We simulate  $n = 4$  qubits. The fidelities quoted in this paper are numerically exact for the model (7); the rotating-wave approximation is not used.

TABLE II. Device parameters used in this work.

Quantity	Value
Empty qubit parking frequency $\omega_{\text{park}}/2\pi$	10.0 GHz
Memory resonator $m_1$ frequency $\omega_{m1}/2\pi$	8.3 GHz
Memory resonator $m_2$ frequency $\omega_{m2}/2\pi$	8.2 GHz
Memory resonator $m_3$ frequency $\omega_{m3}/2\pi$	8.1 GHz
Memory resonator $m_4$ frequency $\omega_{m4}/2\pi$	8.0 GHz
Initial detuned qubit frequency $\omega_{\text{off}}/2\pi$	7.5 GHz
Bus resonator frequency $\omega_b/2\pi$	6.5 GHz
Qubit-memory coupling strength $g_m/2\pi$	100 MHz
Qubit-bus coupling strength $g_b/2\pi$	30–60 MHz
Qubit anharmonicity $\eta/2\pi$	200–400 MHz



Although the CZ and MOVE gates considered here do not involve microwave pulses, the single-qubit gates are assumed to be implemented with microwaves in the usual manner at the qubit frequency  $\omega_{\text{off}}$ . This frequency is also used to define an experimental “rotating” reference frame or local clock for each qubit: All qubit frequencies are defined relative to  $\omega_{\text{off}}$  [33]. This is discussed below in Sec. III C.

### B. Strauch CZ gate

In this section we give a detailed description of the CZ gate introduced by Strauch *et al.* [42]. In particular, we explain the specific roles played by the two pulse-shape parameters  $t_{\text{on}}$  and  $\omega_{\text{on}}$ , and by the two auxiliary  $z$  rotation angles  $\gamma_1$  and  $\gamma_2$ . To accomplish this we introduce several approximations that allow for an analytic treatment of the CZ gate dynamics.

First, we consider a truncated model consisting of a single superconducting qubit with frequency  $\epsilon$  and anharmonic detuning  $\eta$ , capacitively coupled to a bus resonator with frequency  $\omega_b$ ,

$$H = \begin{pmatrix} 0 & 0 & 0 \\ 0 & \epsilon & 0 \\ 0 & 0 & 2\epsilon - \eta \end{pmatrix}_q + \begin{pmatrix} 0 & 0 & 0 \\ 0 & \omega_b & 0 \\ 0 & 0 & 2\omega_b \end{pmatrix}_b + g_b Y_q \otimes Y_b. \quad (9)$$

In this case  $Y$  reduces to

$$Y = \begin{pmatrix} 0 & -i & 0 \\ i & 0 & -\sqrt{2}i \\ 0 & \sqrt{2}i & 0 \end{pmatrix}. \quad (10)$$

This Hamiltonian is written in the basis of *bare* eigenstates, which are the system eigenfunctions when the qubit and resonator are uncoupled. We write these bare states as  $|qb\rangle$ , with  $q, b \in \{0, 1, 2\}$ . The energies of the interacting eigenstates, which we write with an overline as  $\overline{|qb\rangle}$ , are plotted in Fig. 3 as a function of  $\epsilon/2\pi$  for the case of  $\omega_b/2\pi = 6.5$  GHz,  $\eta/2\pi = 300$  MHz, and  $g_b/2\pi = 45$  MHz. The interacting eigenstates are labeled such that  $\overline{|qb\rangle}$  is perturbatively connected to  $|qb\rangle$  when  $\epsilon \gg \omega_b$ .

Second, we assume a short switching time and ignore the dynamical phases acquired during the ramps. As we will see below, this approximation is valid when  $g_b \ll \eta$ , so that the switching can be made *sudden* with respect to the coupling  $g_b$ , but still adiabatic with respect to the anharmonicity  $\eta$ .

The CZ gate of Strauch *et al.* [42], adapted to the qubit-resonator system, works by using the anticrossing of the  $\overline{|11\rangle}$  channel with the auxiliary state  $\overline{|20\rangle}$ . In terms of the pulse parameters defined in (1), the qubit-resonator state is prepared at a qubit frequency  $\epsilon = \omega_{\text{off}}$ , and the frequency is then switched to  $\epsilon = \omega_{\text{on}}$  for a FWHM time duration  $t_{\text{on}}$ . In the simplified model considered in this section,

$$\omega_{\text{on}} = \omega_b + \eta, \quad (11)$$

and

$$t_{\text{on}} = \frac{\pi}{\sqrt{2}g_b}. \quad (12)$$

Equation (11) gives the qubit frequency for which the bare state  $|11\rangle$  is degenerate with  $|20\rangle$ , and is at a frequency  $\eta$  above the

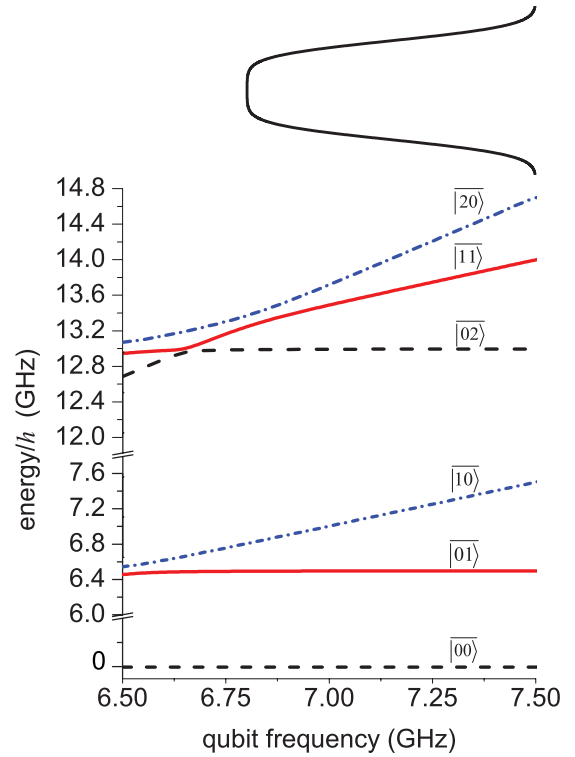


FIG. 3. (Color online) Energies of eigenstates  $\overline{|qb\rangle}$  of a single qubit  $q$  coupled to a resonator bus  $b$ . Here  $\omega_b/2\pi = 6.5$  GHz,  $\eta/2\pi = 300$  MHz, and  $g_b/2\pi = 45$  MHz. The time dependence of the qubit frequency during a CZ gate (solid black curve) is indicated at the top of the figure.

usual resonance condition. Equation (12) is the sudden-limit value defined in (4) and derived below. The qubit frequency is then returned to the detuned value  $\omega_{\text{off}}$ . The complete pulse profile is also shown in Fig. 3 (solid black curve) for the case of  $\omega_{\text{on}}/2\pi = 6.8$  GHz and  $\omega_{\text{off}}/2\pi = 7.5$  GHz.

Let's follow the evolution resulting from an initial (normalized) qubit-resonator state,

$$a_{00}\overline{|00\rangle} + a_{01}\overline{|01\rangle} + a_{10}\overline{|10\rangle} + a_{11}\overline{|11\rangle}. \quad (13)$$

Because the  $\overline{|00\rangle}$  channel is very well separated from the others, the  $\overline{|00\rangle}$  component will only acquire a dynamical phase factor,

$$e^{-iE_{00}t_{\text{gate}}}, \quad (14)$$

where  $E_{00}$  is the energy of the  $\overline{|00\rangle}$  eigenstate. Without loss of generality we can shift the entire spectrum so that  $E_{00} = 0$  [as in (9)] and the phase factor (14) becomes unity. This freedom results from the fact that any unitary gate operation only needs to be defined up to an overall multiplicative phase factor. With this phase convention the CZ gate acts as the identity on this component, so we have the map,

$$\overline{|00\rangle} \rightarrow \overline{|00\rangle}. \quad (15)$$

The  $\overline{|01\rangle}$  component will mostly return to  $\overline{|01\rangle}$ , also with an acquired phase, but a small component will be left in  $\overline{|10\rangle}$  due to the nonadiabatic excitation of that channel, which is only separated in energy from  $\overline{|01\rangle}$  by about  $\eta$  when  $\epsilon = \omega_b + \eta$ . The  $\overline{|10\rangle}$  component similarly suffers from a

small nonadiabatic coupling to  $\overline{|01\rangle}$ . As we will explain below, these nonadiabatic errors are exponentially suppressed when the functional form of  $\epsilon(t)$  is properly designed. Then we have

$$\overline{|01\rangle} \rightarrow e^{-i\alpha} \sqrt{1 - \mathbb{E}_1} \overline{|01\rangle} + e^{-i\alpha'} \sqrt{\mathbb{E}_1} \overline{|10\rangle}, \quad (16)$$

and

$$\overline{|10\rangle} \rightarrow e^{-i\beta} \sqrt{1 - \mathbb{E}_1} \overline{|10\rangle} + e^{-i\beta'} \sqrt{\mathbb{E}_1} \overline{|01\rangle}, \quad (17)$$

where  $\mathbb{E}_1$  is a small nonadiabatic population error (below we refer to  $\mathbb{E}_1$  as a *switching* error). In the  $\mathbb{E}_1 \rightarrow 0$  limit,  $\alpha$  and  $\beta$  are dynamical phases given by

$$\alpha = \int_0^{t_{\text{gate}}} E_{01} dt \approx \left( \omega_b - \frac{g_b^2}{\eta} \right) t_{\text{on}}, \quad (18)$$

$$\beta = \int_0^{t_{\text{gate}}} E_{10} dt \approx \left( \omega_b + \eta + \frac{g_b^2}{\eta} \right) t_{\text{on}}, \quad (19)$$

where the second approximate quantities neglect phase accumulation during the ramps and use perturbative expressions for the energies  $E_{01}$  and  $E_{10}$  when  $\epsilon = \omega_b + \eta$ . The expressions (16) and (17) neglect an extremely small leakage out of the  $\{|01\rangle, |10\rangle\}$  subspace. Neglecting this leakage, the evolution in the  $\{|01\rangle, |10\rangle\}$  subspace is unitary, leading to the phase condition,

$$e^{i(\alpha - \beta')} + e^{i(\alpha' - \beta)} = 0. \quad (20)$$

Using (20) to eliminate  $\beta'$  leads to

$$\overline{|01\rangle} \rightarrow e^{-i\alpha} \sqrt{1 - \mathbb{E}_1} \overline{|01\rangle} + e^{-i(\beta + \phi)} \sqrt{\mathbb{E}_1} \overline{|10\rangle}, \quad (21)$$

$$\overline{|10\rangle} \rightarrow e^{-i\beta} \sqrt{1 - \mathbb{E}_1} \overline{|10\rangle} - e^{-i(\alpha - \phi)} \sqrt{\mathbb{E}_1} \overline{|01\rangle}, \quad (22)$$

where  $\phi \equiv \alpha' - \beta$ . The evolution of the eigenstates  $\overline{|01\rangle}$  and  $\overline{|10\rangle}$  is therefore characterized by the cross-excitation probability  $\mathbb{E}_1$  and three phase angles  $\alpha$ ,  $\beta$ , and  $\phi$ .

Now we consider the  $\overline{|11\rangle}$  component. The  $\overline{|11\rangle}$  channel couples strongly with the  $\overline{|20\rangle}$  channel, as well as weakly with  $\overline{|02\rangle}$ . The simplest way to understand the dynamics of the  $\overline{|11\rangle}$  component is to use two different representations to describe these two effects. We will describe strong interaction with  $\overline{|20\rangle}$  in the bare basis and the weak, nonadiabatic coupling with  $\overline{|02\rangle}$  in the eigenstate basis. Suppose we begin with the qubit strongly detuned from the bus, so that  $\overline{|11\rangle} \approx |11\rangle$  (the detuned interacting eigenstate is well approximated by the bare  $|11\rangle$  state). Then we quickly switch  $\epsilon$  from  $\omega_{\text{off}}$  to  $\omega_b + \eta$ . By “quickly” we mean that we strongly mix with the  $\overline{|20\rangle}$  channel. The interaction with  $\overline{|02\rangle}$  is always weak, even in the sudden limit. This asymmetric excitation is possible because  $\overline{|20\rangle}$  is protected (separated in energy from  $\overline{|11\rangle}$ ) by an energy gap  $2\sqrt{2}g_b$ , whereas  $\overline{|02\rangle}$  is protected by a much larger gap of  $\eta - \sqrt{2}g_b$  (this expression accounts for level repulsion from  $\overline{|20\rangle}$ , and we have assumed that  $g_b \ll \eta$ ). We can informally say that the desired switching is nonadiabatic with respect to the energy scale  $g_b$ , but is adiabatic with respect to  $\eta$  [42].

Focusing first on the strong coupling to  $\overline{|20\rangle}$ , the suddenly switched  $|11\rangle$  state is no longer an eigenstate when  $\epsilon = \omega_{\text{on}}$ , as the relevant eigenfunctions at this setting are

$$\overline{|11\rangle} = \frac{|11\rangle - |20\rangle}{\sqrt{2}} \quad \text{and} \quad \overline{|20\rangle} = \frac{|11\rangle + |20\rangle}{\sqrt{2}}. \quad (23)$$

The nonstationary state

$$|11\rangle = \frac{\overline{|11\rangle} + \overline{|20\rangle}}{\sqrt{2}} \quad (24)$$

therefore rotates in the  $\{|11\rangle, |20\rangle\}$  subspace, and after a time duration  $t$  becomes

$$|\psi\rangle = e^{-iE_{11}t} \left[ \frac{\overline{|11\rangle} + e^{-i\Delta Et} \overline{|20\rangle}}{\sqrt{2}} \right] \quad (25)$$

$$= e^{-iE_{11}t} \left[ \left( \frac{1 + e^{-i\Delta Et}}{2} \right) |11\rangle - \left( \frac{1 - e^{-i\Delta Et}}{2} \right) |20\rangle \right], \quad (26)$$

where

$$\Delta E \equiv E_{20} - E_{11} = 2\sqrt{2}g_b. \quad (27)$$

Holding  $\epsilon$  fixed at  $\omega_b + \eta$  for a FWHM time (12), corresponding to a  $2\pi$  rotation, (26) becomes

$$|\psi\rangle = e^{-iE_{11}t_{\text{on}}} |11\rangle. \quad (28)$$

When  $\epsilon = \omega_b + \eta$ , the energy of eigenstate  $\overline{|11\rangle}$  is

$$E_{11} = 2\omega_b + \eta - \sqrt{2}g_b. \quad (29)$$

After detuning quickly we therefore obtain

$$\overline{|11\rangle} \rightarrow -\exp \left[ -i \left( \pi \frac{2\omega_b + \eta}{\sqrt{2}g_b} \right) \right] \overline{|11\rangle}, \quad (30)$$

or, using expressions (18) and (19),

$$\overline{|11\rangle} \rightarrow -e^{-i(\alpha + \beta)} \overline{|11\rangle}. \quad (31)$$

The two phase angles  $\alpha$  and  $\beta$  can be canceled by the application of independent auxiliary single-qubit  $z$  rotations,

$$R_z(\gamma) \equiv \exp[-i(\gamma/2)\sigma^z], \quad (32)$$

to the qubit and bus. Qubit  $z$  rotations are implemented by frequency excursions, whereas resonator  $z$  rotations are implemented in software (they are compiled into future qubit rotations). Following the pulse sequence that leads to (15), (21), (22), and (31), with the operation,

$$R_z(\gamma_1) \otimes R_z(\gamma_2), \quad (33)$$

where

$$\gamma_1 = -\beta \quad \text{and} \quad \gamma_2 = -\alpha, \quad (34)$$

leads to the map,

$$\overline{|00\rangle} \rightarrow \overline{|00\rangle}, \quad (35)$$

$$\overline{|01\rangle} \rightarrow \sqrt{1 - \mathbb{E}_1} \overline{|01\rangle} + e^{-i\phi} \sqrt{\mathbb{E}_1} \overline{|10\rangle}, \quad (36)$$

$$\overline{|10\rangle} \rightarrow \sqrt{1 - \mathbb{E}_1} \overline{|10\rangle} - e^{i\phi} \sqrt{\mathbb{E}_1} \overline{|01\rangle}, \quad (37)$$

$$\overline{|11\rangle} \rightarrow -\overline{|11\rangle}, \quad (38)$$

apart from a global phase factor. The use of auxiliary  $z$  rotations is discussed further Sec. III D.

The minus sign in (38) is the key to the Strauch CZ gate. However, as mentioned above, the analysis leading to (38) neglected a weak nonadiabatic excitation of the  $\overline{|02\rangle}$  channel caused by the switching of  $\epsilon$ . Including this effect in (38) leads

to the modification,

$$\begin{aligned} |11\rangle &\rightarrow -\sqrt{1 - \mathbb{E}_2} |11\rangle \\ &+ \text{phase factor} \times \sqrt{\mathbb{E}_2} |02\rangle, \end{aligned} \quad (39)$$

where  $\mathbb{E}_2$  is another switching error. Both  $\mathbb{E}_1$  and  $\mathbb{E}_2$  vanish exponentially with  $\sigma$  (or  $t_{\text{ramp}}$ ), and for the regimes studied in this work  $\mathbb{E}_2$  is the dominant source of intrinsic gate fidelity loss. We note that the analysis leading to (39) assumed implementation of the *ideal* values [(11) and (12)] of  $\omega_{\text{on}}$  and  $t_{\text{on}}$ . Errors in these two control parameters, which we refer to as pulse shape errors and study in Sec. III I, lead instead to

$$\begin{aligned} |11\rangle &\rightarrow -e^{i\delta} \sqrt{1 - \mathbb{E}_2 - \mathbb{E}_\theta} |11\rangle \\ &+ \text{phase factor} \times \sqrt{\mathbb{E}_2} |02\rangle \\ &+ \text{phase factor} \times \sqrt{\mathbb{E}_\theta} |20\rangle, \end{aligned} \quad (40)$$

where the controlled-phase error angle  $\delta$  and rotation error  $\mathbb{E}_\theta$  depend on the errors in  $\omega_{\text{on}}$  and  $t_{\text{on}}$ , respectively.

Finally, it is also interesting to consider the fully adiabatic limit of the Strauch CZ gate. By this we mean that the switching is adiabatic with respect to both  $g_b$  and  $\eta$ . For the gate time to be competitive with the nonadiabatic gate of Table I, a larger coupling  $g_b$  is required, which might lead to significant higher-order and cross-coupling errors in a multiqubit device, but in the fully adiabatic limit only *one* pulse control parameter—either  $\omega_{\text{on}}$  or  $t_{\text{on}}$ —needs to be optimized (two  $z$  rotations are still required). This is because adiabaticity now assures that the  $|11\rangle$  population is preserved (apart from exponentially small switching errors), taking over the role previously played by  $t_{\text{on}}$ , and a single pulse shape parameter is sufficient to specify the controlled phase. A highly adiabatic CZ gate was demonstrated in Ref. [43].

There are a few important differences between the Strauch CZ gate applied to a pair of directly coupled qubits (as in Ref. [42]) and to the qubit-bus system considered here. These differences result from the harmonic spectrum of the resonator in the latter case and are discussed below in Sec. IV C.

### C. Eigenstate basis

The Hamiltonian (7) is written in the usual *bare* basis of uncoupled system eigenstates, but information processing itself is best performed in the basis of *interacting* eigenfunctions of  $H_{\text{idle}}$ , where  $H_{\text{idle}}$  is given by (7) with the qubits in a dispersive idling configuration [34]. This choice of computational basis assures that idling states suffer no population change in the decoherence-free limit, and evolve in phase in a way that can be almost exactly compensated for by an appropriate choice of only  $n$  rotating frames or local clocks, one for each qubit [34]. Here we briefly review this important concept.

In principle, any complete orthonormal basis of the physical Hilbert space that can be appropriately prepared, unitarily transformed, and measured—essentially, any basis where one can implement the DiVincenzo criteria [55]—is a valid basis on which to run a quantum computation. Defining the computational states to be interacting system eigenfunctions gives them the simplifying property that the time evolution can be decomposed into a sequence of gates, between which (almost) no evolution occurs. In other words, idling between gates generates the identity operation. This property,

which is implicitly assumed in the standard circuit model of quantum computation, could be realized in an architecture where the Hamiltonian  $H$  can be completely switched off between gates. However, it is not possible to set  $H = 0$  in the QVN architecture; nor can  $H$  itself be made negligibly small between gates. Therefore, nonstationary states such as uncoupled-qubit eigenstates accumulate errors (including population oscillations) between gates unless a correction protocol such as dynamical decoupling [56] is used. By defining computational states in terms of interacting system eigenfunctions  $\{|\psi\rangle\}$  at some predefined dispersive idling configuration (qubit frequencies), the only evolution occurring during an idle from time  $t_1$  to  $t_2$  is a pure phase evolution,

$$|\psi(t_1)\rangle \rightarrow |\psi(t_2)\rangle = e^{-iE(t_2-t_1)} |\psi(t_1)\rangle, \quad (41)$$

where  $E$  is the exact energy eigenvalue (and we neglect decoherence). Furthermore, it is possible to *compensate* for—or effectively remove—the pure phase evolution in (41) by applying phase shifts (after the idle period) to each eigenfunction to cancel the  $e^{-iE(t_2-t_1)}$  phase factors; doing so would result in the ideal between-gate evolution

$$|\psi(t_1)\rangle \rightarrow |\psi(t_2)\rangle = |\psi(t_1)\rangle. \quad (42)$$

The idling dynamics (42) is evidently equivalent to setting  $H = 0$  between gates. We will discuss below how the compensating phase shifts are actually implemented in practice.

This use of interacting system eigenfunctions and compensating phase shifts as described above provides a computational basis that evolves ideally between gates, but such an approach is not scalable; for example, there are  $2^{2n+1}$  such computational states in  $\text{QVN}_n$ . In Ref. [34] an approximate but scalable implementation of this approach was introduced. The idea is that the exact energy  $E$  of a computational state in  $\text{QVN}_n$  is, to an extremely good approximation, the sum of uncoupled qubit and resonator frequencies, i.e., essentially noninteracting. This is *not* simply a consequence of the dispersive regime energies (eigenvalues of  $H_{\text{idle}}$ ), which have non-negligible interaction corrections, but because only a special subset of the eigenfunctions are used for information processing: In the  $\text{QVN}_n$  system we only make use of  $H_{\text{idle}}$  eigenfunctions in which there are no more than  $n$  excitations present, and such that two directly coupled elements—qubits or resonators—are not simultaneously occupied (except during the CZ gate). For example, when the data is stored in memory, the residual memory-memory coupling is fourth order in the qubit-resonator coupling  $g$  (for simplicity we assume here that  $g_b = g_m$ ). This leads to an eighth-order *conditional* frequency shift (order  $g^{16}$  idling error) [34]. Next, suppose an excitation is transferred from memory to a qubit via a MOVE gate. Now the dominant frequency shift is sixth order. And when an excitation is in the bus the largest shift is fourth order [34]. The largest idling error (associated with the phase compensation) is therefore eighth order in  $g$  and can be made negligible with proper system design.

The compensating phase shifts could be implemented through additional local  $z$  rotations, one for each qubit and resonator. However, these phase shifts evolve in time with very high ( $>1$  GHz) frequency, and it is therefore experimentally more practical to introduce a local clock or rotating frame for each qubit and resonator. This is achieved by introducing a

fixed-frequency microwave line for each qubit and resonator, and measuring each qubit and resonator *phase* relative to the phase of its reference. By choosing the frequency of the qubit (resonator) reference microwave equal to the idle frequency (resonator frequency), the component frequencies [and therefore the quantity  $E$  in (41)] are effectively zeroed, and no more than  $2n + 1$  different reference frequencies or local clocks are required. This procedure corresponds to implementing the experiment in a multiqubit rotating frame. And, in a further simplification, the local clocks (or rotating frames) for the resonators are replaced by additional qubit  $z$  rotations that are handled in software (i.e., combined with future rotations). Therefore, in practice only  $n$  local clocks are needed, one for each qubit.

Because the CZ gate simulations reported in Table I are already supplemented with local  $z$  rotations, these local clocks do not need to be included in those simulations; we simulate the laboratory frame. However, they are included in the pulse-shape error simulations reported after (94) and in the  $\text{cz}_{23}$  qubit-qubit gate simulation reported in Sec. IV B.

Having motivated the use of interacting system eigenfunctions for computational basis states, it is still necessary to establish that such states can actually be prepared and measured. Because we can assume the processor to initially start in its interacting ground state—a computational basis state—preparation of the other computational states can be viewed as a series of  $\pi$  pulses and MOVE gates. We expect that such operations on the interacting eigenfunctions can be performed at least as accurately as when applied to bare states. Eigenfunction readout is a more subtle (and model-dependent) question, but the analysis of Ref. [34] suggests that interacting-eigenfunction readout is actually better than bare-state readout (in the model considered there).

We also note that the idling configuration and associated eigenstate basis generally changes between consecutive gates (an example is given below in Sec. IV B). In Table I, the idling configuration has qubit  $q_1$  at  $\omega_{\text{off}}$  and the others at  $\omega_{\text{park}}$ . Therefore, our entangling gate design is constrained by the requirement that we start and end in eigenstates of this particular  $H_{\text{idle}}$ .

The discussion above motivating the use of interacting eigenstates is based on their nearly ideal idling dynamics. It is still interesting, however, to consider whether the CZ gate can be generated equally well in either (bare or interacting eigenfunction) basis. We find that for the parameter regimes considered here, it is not possible to achieve better than about 99% fidelity in the bare basis with the same two-parameter pulse profile (it should be possible using more complex pulse shapes). The residual error is consistent with the size of the perturbative corrections to the bare states in the idling configuration. This exercise emphasizes the importance of performing quantum logic with the system eigenfunctions, which have the built-in protection of *adiabaticity* against unwanted transitions.

One might object to the use of interacting eigenfunctions as a design tool, the exact calculation of which is not scalable. However, approximate dispersive-regime eigenfunctions are efficiently computable. A particularly simple way to do this is to calculate the generator  $S$  of the diagonalizing transformation  $V = e^{-iS}$  by a power series in  $g_b$  and  $g_m$ . At the 99.99% fidelity

level, it is sufficient to calculate  $S$  to first order. Writing  $H_{\text{idle}} = H_0 + \delta H$  leads to the condition  $i[S, H_0] + \delta H = 0$ , which is immediately solvable in the bare basis  $|q_1 q_2 \cdots m_1 m_2 \cdots b\rangle$ . Here  $q_i, m_i, b \in \{0, 1, 2, \dots\}$ . Other efficient eigenfunction approximation schemes are also possible.

In this work we denote the exact or approximate  $H_{\text{idle}}$  eigenfunction perturbatively connected to the bare state  $|q_1 q_2 \cdots q_n m_1 m_2 \cdots m_n b\rangle$  by

$$\overline{|q_1 q_2 \cdots q_n m_1 m_2 \cdots m_n b\rangle}, \quad (43)$$

following the overline notation introduced above. Note that (43) is *not* a tensor product of single-qubit and resonator eigenstates as is usually the case.

#### D. Auxiliary $z$ rotations and CZ equivalence class

The standard CZ gate in the bare two-qubit basis  $\{|00\rangle, |01\rangle, |10\rangle, |11\rangle\}$  is

$$\text{CZ} \equiv \begin{pmatrix} 1 & 0 & 0 & 0 \\ 0 & 1 & 0 & 0 \\ 0 & 0 & 1 & 0 \\ 0 & 0 & 0 & -1 \end{pmatrix}. \quad (44)$$

However, in the QVN processor, local  $z$  rotations can be performed quickly and accurately, typically by brief qubit frequency excursions. Thus, we will consider the limit where  $\text{SU}(2)$  operations of the form  $\exp[-i(\theta/2)\sigma^z]$  can be done on the qubits and bus with negligible error and in a negligible amount of time (fidelity loss resulting from errors in these rotations are discussed in Sec. III I). We therefore want to define our entangling gate modulo these  $z$  rotations. We will do this by constructing a *local- $z$  equivalence class* for an arbitrary element (gate) in  $\text{SU}(4)$ , and then specialize to the CZ gate.

We define two elements  $U$  and  $U'$  of  $\text{SU}(4)$  to be equivalent, and write  $U' \doteq U$ , if

$$U' = u_{\text{post}} U u_{\text{pre}}, \quad (45)$$

where

$$u(\gamma_1, \gamma_2) \equiv R_z(\gamma_1) \otimes R_z(\gamma_2) = e^{i(\gamma_1 + \gamma_2)/2} \begin{pmatrix} 1 & 0 & 0 & 0 \\ 0 & e^{-i\gamma_2} & 0 & 0 \\ 0 & 0 & e^{-i\gamma_1} & 0 \\ 0 & 0 & 0 & e^{-i(\gamma_1 + \gamma_2)} \end{pmatrix}, \quad (46)$$

for some rotation angles  $\gamma_k$ . The local- $z$  equivalence class  $\{U\}$  corresponding to  $U$  is the set of elements  $u_{\text{post}} U u_{\text{pre}}$  for all  $u_{\text{pre}}, u_{\text{post}}$ . For a given gate  $U$ ,  $\{U\}$  typically occupies a four-dimensional manifold, depending on four rotation angles. But because (44) is diagonal,  $\{\text{CZ}\}$  instead forms a two-dimensional sheet,

$$\{\text{cz}\} = \text{phase factor} \times \begin{pmatrix} 1 & 0 & 0 & 0 \\ 0 & e^{-i\gamma_2} & 0 & 0 \\ 0 & 0 & e^{-i\gamma_1} & 0 \\ 0 & 0 & 0 & -e^{-i(\gamma_1 + \gamma_2)} \end{pmatrix}. \quad (47)$$

The CZ gate (44) can be obtained by reaching any point in the  $\{\text{CZ}\}$  plane and then performing auxiliary  $z$  rotations. And it is



straightforward to confirm that [43]

$$\begin{pmatrix} -1 & 0 & 0 & 0 \\ 0 & 1 & 0 & 0 \\ 0 & 0 & 1 & 0 \\ 0 & 0 & 0 & 1 \end{pmatrix} \stackrel{\circ}{=} \begin{pmatrix} 1 & 0 & 0 & 0 \\ 0 & -1 & 0 & 0 \\ 0 & 0 & 1 & 0 \\ 0 & 0 & 0 & 1 \end{pmatrix} \stackrel{\circ}{=} \begin{pmatrix} 1 & 0 & 0 & 0 \\ 0 & 1 & 0 & 0 \\ 0 & 0 & -1 & 0 \\ 0 & 0 & 0 & 1 \end{pmatrix} \\ \stackrel{\circ}{=} \begin{pmatrix} 1 & 0 & 0 & 0 \\ 0 & 1 & 0 & 0 \\ 0 & 0 & 1 & 0 \\ 0 & 0 & 0 & -1 \end{pmatrix}. \quad (48)$$

We note that bus rotations, which cannot be directly implemented with microwave pulses or frequency excursions, are compiled into future qubit rotations.

The discussion above assumed a pair of qubits or a qubit and resonator, but it applies to a QVN processor in the interacting eigenfunction basis (43) after a minor modification. In the bare basis, the CZ gate is typically defined through its action (44) on a pair of qubits (or a qubit and resonator). Then, action on a bare computational basis state such as  $|q_1 q_2 \cdots q_n m_1 m_2 \cdots m_n b\rangle$  follows from the tensor-product form of that bare state. In the eigenstate basis the CZ gate must be *defined* through its action on

$$|q_1 q_2 \cdots q_n m_1 m_2 \cdots m_n b\rangle, \quad (49)$$

such as to reproduce the ideal action on the bare states to which they are perturbatively connected. For example, the CZ gate on qubit  $q_1$  and the bus acts ideally as

$$\begin{aligned} \text{CZ} |0q_2q_3q_4m_1m_2m_3m_40\rangle &= |0q_2q_3q_4m_1m_2m_3m_40\rangle \\ \text{CZ} |0q_2q_3q_4m_1m_2m_3m_41\rangle &= |0q_2q_3q_4m_1m_2m_3m_41\rangle \\ \text{CZ} |1q_2q_3q_4m_1m_2m_3m_40\rangle &= |1q_2q_3q_4m_1m_2m_3m_40\rangle \\ \text{CZ} |1q_2q_3q_4m_1m_2m_3m_41\rangle &= -|1q_2q_3q_4m_1m_2m_3m_41\rangle, \end{aligned}$$

where  $q_i, m_i \in \{0, 1, 2, \dots\}$ .

### E. Fidelity definitions

The gate or process fidelity measure we use in this work is based on a state fidelity defined by the inner product of the ideal and realized final (pure) states, squared. This leads to a state-averaged fidelity given by [57,58]

$$F_{\text{ave}}(U, U_{\text{target}}) \equiv \frac{\text{Tr}(U^\dagger U) + |\text{Tr}(U_{\text{target}}^\dagger U)|^2}{20}, \quad (50)$$

where  $U$  is the realized time-evolution operator in the interacting eigenfunction basis after auxiliary  $z$  rotations, projected into the relevant computational subspace, and  $U_{\text{target}} = \text{CZ}$  [see (44)]. Note that the *projected*  $U$  is not necessarily unitary here, and that the first term in (50) characterizes the possible leakage from the computational basis (nonunitarity) whereas the second term is proportional to the square of the Hilbert-Schmidt inner product of  $U$  with  $U_{\text{target}}$ . Although  $U$  is not assumed to be unitary, the expression (50) assumes a pure state and is (obviously) not valid in the presence of decoherence. [The formula (50) assumes that the Kraus representation for the completely positive process is not necessarily trace preserving, but it has only one term.] The form (50) also assumes an

average over a four-dimensional Hilbert space; in the  $N$ -dimensional generalization the denominator is  $N + N^2$ , which is necessary (note numerator) to assure that  $F_{\text{ave}}(U_{\text{target}}, U_{\text{target}})$  is unity.

It is also useful to calculate the minimum or worst-case fidelity. The minimum fidelity of interest here is the state fidelity *minimized* over initial computational states, for a gate that has already been optimized (by maximizing  $F_{\text{ave}}$ ). In Sec. III B we argued that the dominant intrinsic error mechanism (for an optimal pulse) in the truncated qubit-resonator model (9) is the nonadiabatic excitation of the  $|02\rangle$  channel, in which there are two photons left in the bus resonator. Therefore, in the model (9), the minimum state fidelity occurs for the initial eigenstate  $|11\rangle$ . In the QVN<sub>4</sub> processor, this worst-case state is written [in the notation of (43)] as

$$|100000001\rangle, \quad (51)$$

where we have assumed a CZ gate between qubit  $q_1$  and the bus. Numerical simulation of this gate in the QVN<sub>4</sub> processor confirms that the minimum CZ fidelity indeed occurs for the initial state (51), and is due to leakage from the computational subspace. We therefore define the minimum fidelity to be the state fidelity for initial condition (51),

$$F_{|11\rangle} \equiv |\langle 100000001 | U | 100000001 \rangle|^2. \quad (52)$$

Note that this expression is not sensitive to the value of the controlled phase, and only accounts for leakage from the computational subspace. Simulated values of  $F_{|11\rangle}$  for the qubit-bus CZ gate are given in Table I, along with estimates of this same quantity that are discussed below in Sec. III H.

### F. Pulse shape

In the QVN Hamiltonian (7), the qubit frequencies  $\epsilon_i$  are the only available experimental controls. [There are also single-qubit terms for microwave pulses that are not shown in (7) and not used in this work.] During a CZ gate between a given qubit and the resonator bus, the frequency of that qubit is varied according to (1), where

$$\text{Erf}(t) \equiv \frac{2}{\sqrt{\pi}} \int_0^t e^{-x^2} dx, \quad (53)$$

with the other qubits remaining at the parking frequency  $\omega_{\text{park}}$  (given in Table II).

Two quantities related to the pulse switching— $\sigma$  and  $t_{\text{ramp}}$ —appear in the pulse profile function (1). We do this to emphasize that, in principle, two independent quantities could be used to quantify the shape of the switching profile. The first is the time duration (or width) of the switching, characterized by the standard deviation  $\sigma$ . The second is the truncation time of the pulse, measured from the center (half maximum) of the frequency switch, which is equal to  $t_{\text{ramp}}/2$ . However, in this work we always use the (somewhat arbitrary) relation (2), which amounts to cutting off the pulse at  $2\sqrt{2}$  standard deviations from the switching midpoints.

If the pulse shape function (1) is used only when  $0 \leq t \leq t_{\text{gate}}$ , and  $\epsilon$  is set to  $\omega_{\text{off}}$  otherwise, there will be small pulse discontinuities at  $t = 0$  and  $t_{\text{gate}}$ , the size of which is determined by the condition (2). Assuming  $t_{\text{ramp}} \ll t_{\text{gate}}$ , we

have

$$\epsilon(0) = \epsilon(t_{\text{gate}}) \approx \omega_{\text{off}} + \frac{\omega_{\text{on}} - \omega_{\text{off}}}{2} [1 - \text{Erf}(2)], \quad (54)$$

which differs from the asymptotic value  $\omega_{\text{off}}$  by an amount,

$$\frac{\omega_{\text{on}} - \omega_{\text{off}}}{2} [1 - \text{Erf}(2)], \quad (55)$$

where  $1 - \text{Erf}(2) \approx 0.5\%$ . However, in an experiment these discontinuities are usually smoothed over by additional pulse shaping. Moreover, our simulations begin at  $t = 0$  and end at  $t = t_{\text{gate}}$ , so the truncation only slightly affects the pulse shape: The initial and final detuned qubit frequency is actually a few MHz smaller than  $\omega_{\text{off}}$ .

Having fixed the relation (2), there are then two measures of the pulse switching time,  $\sigma$  and  $t_{\text{ramp}}$ , with  $t_{\text{ramp}}$  providing a convenient measure of the time duration of the ramps. This property can be seen in the pulse shape example of Fig. 2.

### G. Gate optimization

We numerically optimize the two pulse-shape control parameters  $\omega_{\text{on}}$  and  $t_{\text{on}}$ , as well as the two auxiliary  $z$  rotation angles,  $\gamma_1$  and  $\gamma_2$ , to maximize the average gate fidelity (50). All other pulse parameters ( $\omega_{\text{off}}$ ,  $\sigma$ ,  $t_{\text{ramp}}$ ) are fixed. The values of  $\omega_{\text{off}}$  and  $t_{\text{ramp}}$  are determined by the system optimization analysis of Sec. V, and then  $\sigma$  is obtained through relation (2). The roles played by the control parameters  $\omega_{\text{on}}$  and  $t_{\text{on}}$  are discussed above in Sec. III B.

The fidelity optimization procedure is carried out in two stages: In the first stage we take  $\omega_{\text{on}}$  to be equal to its approximate value [see (11)],

$$\omega_b + \eta, \quad (56)$$

and optimize  $t_{\text{on}}$  to get close to the two-dimensional equivalence class {CZ} defined in (47). We do this by minimizing a sum of two positive errors, one measuring the deviation of the absolute values of the matrix elements of the evolution operator  $U$  (projected into the  $q_1$ - $b$  subspace) from that of the four-dimensional identity matrix, the other measuring the deviation from the ideal relationship between the phases of the diagonal elements indicated in (47). This first stage yields an approximate value of  $t_{\text{on}}$ , as well as approximate rotation angles,

$$\gamma_1 \approx \arg \langle 10|U|10 \rangle - \arg \langle 00|U|00 \rangle, \quad (57)$$

$$\gamma_2 \approx \arg \langle 01|U|01 \rangle - \arg \langle 00|U|00 \rangle. \quad (58)$$

In the second stage of optimization, we use the approximate values of  $\omega_{\text{on}}$ ,  $t_{\text{on}}$ ,  $\gamma_1$ , and  $\gamma_2$ , obtained from the first stage, as seeds for a full four-dimensional ( $\omega_{\text{on}}$ ,  $t_{\text{on}}$ ,  $\gamma_1$ ,  $\gamma_2$ ) nonlinear maximization of the average fidelity (50) between

$$u(\gamma_1, \gamma_2) \times U, \quad (59)$$

and the standard CZ gate (44). Here  $U$  is the projected evolution operator and  $u \in \text{SU}(2) \otimes \text{SU}(2)$  is defined in (46).

There are two obvious approaches to simulating the gate evolution in the interacting eigenfunction basis (43). The first is to use the appropriate  $H_{\text{idle}}$  eigenstates to transform the target gate (44) to the bare basis, and perform the actual simulation in the bare basis. However, this approach requires

that the subspace projection operators—which are naturally defined in the eigenstate basis—also be transformed. The second approach, which we follow here, is to transform the QVN Hamiltonian (7) to the eigenstate basis and perform the simulation in that basis.

### H. Switching error and fidelity estimate

In this section we calculate the transition probability caused by a change of the qubit frequency during a CZ pulse, MOVE gate, or any other operation in the QVN system or related superconducting architectures. The problem will be treated quite generally and then applied to the Strauch CZ gate of Table I, resulting in a simple fidelity estimator for that gate. The quantities  $A$ ,  $p_{\text{sw}}$ , and  $F_{11}^{(\text{est})}$  appearing in Table I are discussed in this section.

Imagine that we have prepared an initial interacting system eigenfunction  $|\bar{a}\rangle$  prior to performing a CZ operation or other gate that involves changing the frequency of one or more qubits. We assume that the ideal (target) behavior during the frequency switch or ramp itself is the *identity* map (times a phase factor), and that the  $|\bar{a}\rangle$  channel does not cross any others in the system. The population loss during the ramp will therefore be exponentially suppressed if the switching time is long enough.

In a multiqubit system there is typically a large number of nonresonant channels coupled to  $|\bar{a}\rangle$  that can be excited by the frequency switch. However, when the ramp fidelity is high and the probabilities of the undesired transitions,

$$|\bar{a}\rangle \rightarrow |\bar{b}\rangle, |\bar{b}'\rangle, |\bar{b}''\rangle, \dots, \quad (60)$$

are small, they can be individually estimated perturbatively (neglecting interference), thereby reducing the problem to a sum of independent two-channel problems,

$$\begin{aligned} |\bar{a}\rangle &\rightarrow |\bar{b}\rangle, \\ |\bar{a}\rangle &\rightarrow |\bar{b}'\rangle, \\ |\bar{a}\rangle &\rightarrow |\bar{b}''\rangle, \\ &\vdots \end{aligned} \quad (61)$$

each characterized by a time-dependent detuning  $\Delta$  and a coupling  $G$ . Without loss of generality we can shift the energy of a given two-channel problem so that the bare final state has zero energy. Each nonadiabatic transition can therefore be described by a general two-channel model of the form,

$$H = \begin{pmatrix} \Delta(t) & G \\ G & 0 \end{pmatrix}, \quad (62)$$

in the bare basis spanned by  $\{|a\rangle, |b\rangle\}$ . The undesired final state  $|b\rangle$  has a fixed energy 0 and the energy of  $|a\rangle$  varies in time with detuning  $\Delta$ . The coupling  $G$  is assumed to be a real, positive constant.

The instantaneous eigenstates of (62) are

$$|\bar{a}\rangle = \cos \frac{\chi}{2} |a\rangle + \sin \frac{\chi}{2} |b\rangle, \quad (63)$$

$$|\bar{b}\rangle = \cos \frac{\chi}{2} |b\rangle - \sin \frac{\chi}{2} |a\rangle, \quad (64)$$

where

$$\chi \equiv \arctan\left(\frac{2G}{\Delta}\right). \quad (65)$$

The instantaneous energies are

$$E_a = \frac{\Delta}{2} + \sqrt{\left(\frac{\Delta}{2}\right)^2 + G^2}, \quad (66)$$

and

$$E_b = \frac{\Delta}{2} - \sqrt{\left(\frac{\Delta}{2}\right)^2 + G^2}. \quad (67)$$

The  $|\bar{b}\rangle$  channel is initially unoccupied at time  $t = 0$ , and we are interested in the probability  $p_{\text{sw}}$  that the system, prepared in  $|a\rangle$ , is found in  $|\bar{b}\rangle$  after changing the detuning  $\Delta$  from one value to another. We refer to this probability as the nonadiabatic switching error, which we calculate by expanding the wave function in the basis of instantaneous eigenstates (63) and (64), as

$$|\psi\rangle = \sum_{m=a,b} \psi_m e^{-i \int_0^t E_m d\tau} |\bar{m}\rangle. \quad (68)$$

This leads to

$$\frac{d\psi_b}{dt} = -e^{-i \int_0^t (E_a - E_b) d\tau} \langle \bar{b} | \frac{\partial}{\partial \Delta} | a \rangle \frac{d\Delta}{dt} \psi_a, \quad (69)$$

where

$$\langle \bar{b} | \frac{\partial}{\partial \Delta} | a \rangle = -\frac{G}{\Delta^2} \times \frac{1}{1 + \left(\frac{2G}{\Delta}\right)^2}. \quad (70)$$

The nonadiabatic matrix element (70) has been written so that the second term approaches unity in the  $G \ll \Delta$  perturbative limit.

At time  $t = 0$ ,  $\psi_a = 1$ . An approximate expression for

$$p_{\text{sw}} \equiv |\psi_b(t_{\text{final}})|^2 \quad (71)$$

can be obtained from (69) by assuming that  $|\psi_b| \ll 1$  throughout the evolution, so that  $\psi_a \approx 1$  for all  $t$ . Then,

$$p_{\text{sw}} = \left| \int \frac{G \dot{\Delta} e^{-i \int_0^t \Omega d\tau}}{\Omega^2} dt \right|^2 = \frac{1}{4} \left| \int \dot{\chi} e^{-i \int_0^t \Omega d\tau} dt \right|^2, \quad (72)$$

where

$$\Omega \equiv E_a - E_b = \sqrt{\Delta^2 + 4G^2} \quad (73)$$

is the instantaneous splitting. We can simplify (72) further by assuming  $G \ll \Delta$ , which will be the case for the applications considered below. In this perturbative limit we therefore obtain

$$p_{\text{sw}} = \left| \int \frac{G \dot{\Delta}}{\Delta^2} e^{-i \int_0^t \Delta d\tau} dt \right|^2. \quad (74)$$

We emphasize that the form (74) assumes that  $\Delta$  does not pass through zero, which would cause Landau-Zener tunneling and invalidate the perturbative analysis.

In this work we are specifically interested in  $p_{\text{sw}}$  for a single switch of the detuning from  $\Delta_{\text{on}}$  to  $\Delta_{\text{off}}$  (or the reverse) according to the smooth, error-function based profile,

$$\Delta(t) = \frac{\Delta_{\text{off}} + \Delta_{\text{on}}}{2} + \frac{\Delta_{\text{off}} - \Delta_{\text{on}}}{2} \text{Erf}\left(\frac{t - \frac{1}{2}t_{\text{ramp}}}{\sqrt{2}\sigma}\right), \quad (75)$$

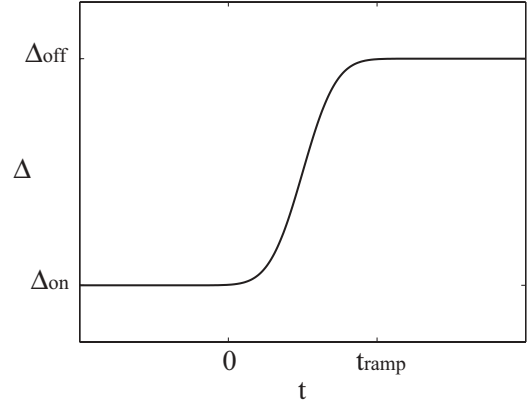


FIG. 4. Detuning pulse profile (75) for a single frequency switch.

shown in Fig. 4. The standard deviation  $\sigma$  characterizes the switching time of the pulse and  $t_{\text{ramp}}$  [related to  $\sigma$  through (2)] specifies its truncation, as discussed in Sec. III F. We use this switching profile for both CZ and MOVE gates. The switching error for the single switch profile defined in (75) and shown in Fig. 4 can be expressed as

$$p_{\text{sw}} = \left(\frac{G}{\Delta_{\text{on}}}\right)^2 |A|^2, \quad (76)$$

where

$$A(\Delta_{\text{on}}, \Delta_{\text{off}}, \sigma) \equiv \Delta_{\text{on}} \int_0^{t_{\text{ramp}}} \frac{\dot{\Delta}}{\Delta^2} e^{-i \int_0^t \Delta d\tau} dt. \quad (77)$$

The dimensionless quantity  $|A|^2$  is plotted in Fig. 5 for five instances of  $\Delta_{\text{on}}$  and  $\Delta_{\text{off}}$  relevant to this work. We note that  $p_{\text{sw}}$  evidently decreases as an exponential function of  $\sigma$ , as expected for a nonadiabatic process. However, the dependence of  $|A|^2$  on  $\sigma$  for large  $\sigma$  is somewhat intricate, a consequence of the error-function ramp shape. For very large values of  $\sigma$ —not shown in Fig. 5—the decay of  $|A|^2$  becomes slower (the location of the crossover depends on the details of the pulse truncation). Although an approximate analytic expression for  $|A|^2$  can be derived for this large- $\sigma$  limit, the formula is not useful for the regimes of interest here.

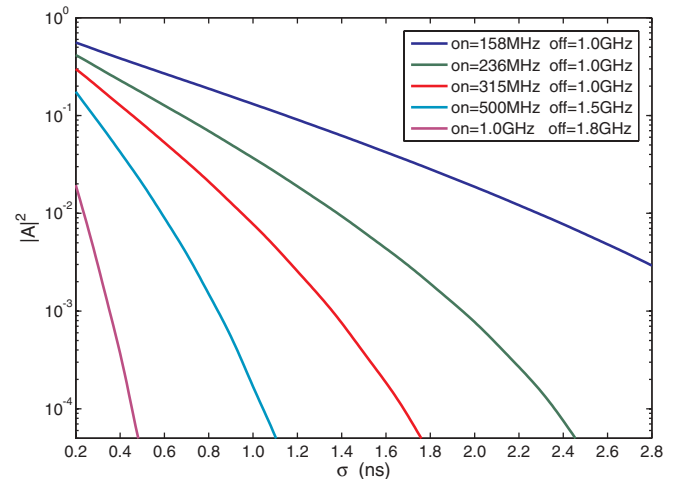


FIG. 5. (Color online)  $|A|^2$  versus switching time  $\sigma$  for indicated values of  $\Delta_{\text{on}}$  and  $\Delta_{\text{off}}$ .

We now turn to the application of the switching error formula (76) to the CZ gate of Table I. As we have explained above in Sec. III E, the initial condition in the QVN<sub>4</sub> processor with the minimum fidelity after a CZ gate (between qubit  $q_1$  and the bus) is the eigenstate (51). For a perfect CZ gate this state would map to

$$-\overline{|100000001\rangle}, \quad (78)$$

but in practice we will find population in other channels as well, the dominant error (for an optimal pulse) occurring in  $\overline{|000000002\rangle}$ , which has two excitations in the bus. This dominant error mechanism involves only a single qubit and resonator, and can be understood entirely within the truncated model (9). In the language of that model, where the bare states (interacting eigenstates) are written as  $|qb\rangle$  ( $|\overline{qb}\rangle$ ), the dominant fidelity loss of the  $\overline{|11\rangle}$  eigenstate is caused by nonadiabatic leakage to  $\overline{|02\rangle}$ . We call this leakage error  $\mathbb{E}_2$ .

It is possible to understand this dominant  $\overline{|11\rangle} \rightarrow \overline{|02\rangle}$  leakage error in a further simplified two-channel model that only includes the channels  $\overline{|11\rangle}$  and  $\overline{|02\rangle}$ . Given the strong interaction of the bare  $|11\rangle$  state with  $|20\rangle$ , it is not at all obvious that such a simplification is possible. However, during most of the switching, the detuning between  $|11\rangle$  and  $|20\rangle$  is much larger than their interaction strength  $\sqrt{2}g_b$ , so they are effectively decoupled. (And while the qubit sits at the  $\omega_{\text{on}}$  frequency, the Hamiltonian is time independent.) Therefore a two-channel description should be possible, although it will slightly overestimate the excitation of  $\overline{|02\rangle}$ . Numerical investigation confirms that the  $|20\rangle$  channel can indeed be disregarded except for the level repulsion it produces on the  $\overline{|11\rangle}$  state (see below), which is crucial for obtaining an accurate fidelity estimate.

In the bare  $\{|11\rangle, |02\rangle\}$  basis, (9) reduces to

$$H = \begin{pmatrix} \epsilon & \sqrt{2}g_b \\ \sqrt{2}g_b & \omega_b \end{pmatrix} + \text{const.} \quad (79)$$

At the beginning of the CZ pulse of Table I, the qubit frequency is 1.0 GHz above the bus.  $\epsilon$  then decreases to  $\omega_{\text{on}} \approx \omega_b + \eta$  and returns to the detuned configuration in the manner of Fig. 2. The total leakage to  $\overline{|02\rangle}$  can be estimated as twice—because there are two switching events, which we assume to contribute incoherently—the value of  $p_{\text{sw}}$ . Therefore the error  $\mathbb{E}_2$  introduced in (39) is given by

$$\mathbb{E}_2 = 2p_{\text{sw}}. \quad (80)$$

To evaluate the switching error in this case, we use (76) with the parameter values,

$$G = \sqrt{2}g_b, \quad (81)$$

$$\Delta_{\text{on}} = \eta - \sqrt{2}g_b, \quad (82)$$

$$\Delta_{\text{off}} = \omega_{\text{off}} - \omega_b. \quad (83)$$

The value of  $\Delta_{\text{on}}$  accounts for the level repulsion caused by the neglected  $|20\rangle$  state, which causes the  $\overline{|11\rangle}$  channel to shift downwards towards  $\overline{|02\rangle}$ ; this large effect is evident in Fig. 3. [We ignore here a smaller repulsion by  $\overline{|02\rangle}$ , which would lead to the addition of a small positive correction to (82).]  $\Delta_{\text{off}}/2\pi$  is always 1.0 GHz for the gates listed in Table I. The required

$|A|^2$  values are obtained from Fig. 5 and are provided in Table I along with  $p_{\text{sw}}$ .

The minimum fidelity estimate,

$$F_{\overline{|11\rangle}}^{(\text{est})} \equiv 1 - \mathbb{E}_2 = 1 - 2p_{\text{sw}}, \quad (84)$$

is also given in Table I and compared to simulated QVN<sub>4</sub> values of  $F_{\text{ave}}$  and  $F_{\overline{|11\rangle}}$ . We find that (84) is a reliable predictor of the worst-case fidelity  $F_{\overline{|11\rangle}}$  in QVN<sub>4</sub>, confirming that the nonadiabatic switching error is the dominant fidelity loss mechanism here. Although this error will always be present, it can be exponentially suppressed by increasing the switching time.

Finally, we briefly comment on the nonadiabatic switching errors between the  $\overline{|01\rangle}$  and  $\overline{|10\rangle}$  eigenstates, which we have argued to be subdominant to the excitation of  $\overline{|02\rangle}$ , but which naively are of the same order. There are two reasons why the  $\overline{|01\rangle}$  and  $\overline{|10\rangle}$  switching errors are considerably smaller: First, the matrix element coupling  $\overline{|01\rangle}$  and  $\overline{|10\rangle}$  is a factor of  $\sqrt{2}$  smaller than that between  $\overline{|11\rangle}$  and  $\overline{|02\rangle}$ , and this factor gets squared in (76). And the second—but quantitatively more important—reason is that while level repulsion considerably enhances the  $\overline{|02\rangle}$  excitation [recall (82)], it (slightly) suppresses transitions between  $\overline{|01\rangle}$  and  $\overline{|10\rangle}$ .

We can estimate the switching errors between the  $\overline{|01\rangle}$  and  $\overline{|10\rangle}$  channels during a CZ gate by using (76) with parameters,

$$G = g_b, \quad (85)$$

$$\Delta_{\text{on}} = \eta + \frac{2g_b^2}{\eta}, \quad (86)$$

and with  $\Delta_{\text{off}}/2\pi = 1$  GHz as before. The expression (86) for  $\Delta_{\text{on}}$  accounts for the level repulsion between  $\overline{|01\rangle}$  and  $\overline{|10\rangle}$ , which suppresses the switching error, in contrast with the strong enhancement indicated in (82). Considering, for example, the 99.9% CZ gate of Table I designed for the  $\eta/2\pi = 300$  MHz qubit, we find that  $|A|^2 = 2.2 \times 10^{-3}$  and

$$p_{\text{sw}} = 4.4 \times 10^{-5}. \quad (87)$$

The total error in this case is  $\mathbb{E}_1 = 2p_{\text{sw}}$ . The estimate (87) for the switching error between  $\overline{|01\rangle}$  and  $\overline{|10\rangle}$  is more than an order-of-magnitude smaller than that between  $\overline{|11\rangle}$  and  $\overline{|02\rangle}$ , which is  $p_{\text{sw}} = 1.2 \times 10^{-3}$  (see Table I).

### I. Pulse shape errors

In Sec. III H we discussed the intrinsic error of the qubit-bus CZ gate—assuming an optimal pulse shape—and identified its dominant source as a nonadiabatic switching error  $\mathbb{E}_2$ . In this section we discuss and quantify the fidelity loss caused by pulse shape and auxiliary  $z$  rotation errors. By a pulse shape error we mean that the correct functional form (1) is seen by the qubit, but with values of the parameters  $t_{\text{on}}$  and  $\omega_{\text{on}}$  that deviate from the optimal values. It is possible to develop simple analytic models for these error mechanisms (supported by numerical simulation) by noting that when the fidelity is very close to unity, the different error mechanisms present contribute independently and can be calculated separately. We then use these results to estimate the experimental pulse-control precision required during the implementation of a



given 99.9% or 99.99% CZ gate to keep any accompanying pulse shape error less than the base  $10^{-3}$  or  $10^{-4}$  gate error.

The simplest situation to consider is that where the correct values of  $t_{\text{on}}$  and  $\omega_{\text{on}}$  are used, but where the local  $z$  rotation angles  $\gamma_k$  ( $k = 1, 2$ ) applied experimentally deviate from their optimal values by amounts  $\varphi_k \ll 1$ . We estimate the resulting fidelity loss by imagining that we have achieved a perfect CZ-class gate,

$$U = \begin{pmatrix} 1 & 0 & 0 & 0 \\ 0 & e^{i\Theta_2} & 0 & 0 \\ 0 & 0 & e^{i\Theta_1} & 0 \\ 0 & 0 & 0 & -e^{i(\Theta_1+\Theta_2)} \end{pmatrix}, \quad (88)$$

for some phase angles  $\Theta_k$ , but then apply  $z$  rotation angles,

$$\gamma_k = \Theta_k + \varphi_k, \quad (89)$$

that have errors  $\varphi_k$ . From (50) we find that this leads to a leading order error  $\mathbb{E} \equiv 1 - F_{\text{ave}}$  given by

$$\mathbb{E} = \frac{\varphi_1^2 + \varphi_2^2}{5}. \quad (90)$$

Next we consider  $t_{\text{on}}$  and  $\omega_{\text{on}}$  errors. An error in either  $t_{\text{on}}$  or  $\omega_{\text{on}}$  has two consequences: The first is to modify the accumulated phases  $\Theta_k$  in (88), and the second is to cause population and phase errors on the  $|11\rangle$  channel. Therefore we consider two types of pulse shape errors, the first where  $t_{\text{on}}$  or  $\omega_{\text{on}}$  is changed with no compensating changes in the auxiliary  $z$  rotation angles, and the second where the  $\gamma_k$  are reoptimized.

In the first case, in which the error is clearly the largest, the resulting error is dominated by the  $z$  rotation angle error itself, which can be estimated from (90). Changing  $t_{\text{on}}$  by an amount  $\delta t_{\text{on}}$ , or  $\omega_{\text{on}}$  by an amount  $\delta \omega_{\text{on}}$ , changes the accumulated phase of the qubit (recall discussion of the qubit reference frame in Secs. III A and III C) by

$$\varphi_1 = (\omega_{\text{on}} - \omega_{\text{off}}) \delta t_{\text{on}} + \delta \omega_{\text{on}} t_{\text{on}}, \quad (91)$$

and that of the bus by

$$\varphi_2 = 0. \quad (92)$$

We note that  $\delta t_{\text{on}}$  and  $\delta \omega_{\text{on}}$  can be positive or negative here, and that the total gate time  $t_{\text{gate}}$  is also (slightly) changed by  $\delta t_{\text{on}}$ . The additional accumulated phase (91) can be regarded as a rotation angle error because, by assumption, it is not compensated by the applied  $z$  rotations (hence the notation). The error angle  $\varphi_2$  is zero because of our choice of the local clock (or reference frame) for a resonator. Therefore, an error in either  $t_{\text{on}}$  or  $\omega_{\text{on}}$  with no compensating adjustment of the auxiliary  $z$  rotation angles leads to a leading-order fidelity loss of

$$\mathbb{E} = \frac{(\omega_{\text{off}} - \omega_{\text{on}})^2}{5} \delta t_{\text{on}}^2 + \frac{t_{\text{on}}^2}{5} \delta \omega_{\text{on}}^2. \quad (93)$$

For an order-of-magnitude estimate it is sufficient to approximate  $\omega_{\text{on}}$  here by  $\omega_b$  and  $t_{\text{on}}$  by  $t_{\text{on}}^{\text{sudden}}$  [see (4)], leading to the simpler estimate,

$$\mathbb{E}' = \frac{(\omega_{\text{off}} - \omega_b)^2}{5} \delta t_{\text{on}}^2 + \frac{(t_{\text{on}}^{\text{sudden}})^2}{5} \delta \omega_{\text{on}}^2. \quad (94)$$

Considering the 99.9% CZ gate of Table I designed for the  $\eta/2\pi = 300$  MHz transmon, we estimate from (94) that a 10 ps error in  $t_{\text{on}}$  (or a 1 MHz error in  $\omega_{\text{on}}/2\pi$ ) would lead to a fidelity loss of  $7.9 \times 10^{-4}$  (or  $4.9 \times 10^{-4}$ ), whereas numerical simulation of the same error in QVN<sub>4</sub>, which includes all subdominant processes, yields  $4.5 \times 10^{-4}$  (or  $1.2 \times 10^{-3}$ ).

Next we consider the case where there is an error in  $t_{\text{on}}$  or  $\omega_{\text{on}}$ , but the auxiliary  $z$  rotation angles are optimal. Here the analysis closely follows that of Sec. III B, which is based on the truncated qubit-resonator model (9). In this situation the fidelity loss is dominated by deviations from the ideal evolution,

$$cz|\overline{11}\rangle = -|\overline{11}\rangle, \quad (95)$$

of the  $|\overline{11}\rangle$  channel. Pulse shape errors will lead to both population and phase errors on the right-hand side of (95). We therefore parametrize the nonideal CZ gate by

$$U = \text{phase factor} \times \begin{pmatrix} 1 & 0 & 0 & 0 \\ 0 & 1 & 0 & 0 \\ 0 & 0 & 1 & 0 \\ 0 & 0 & 0 & -e^{i\delta} \cos \frac{\theta}{2} \end{pmatrix}. \quad (96)$$

In (96) we have assumed perfect auxiliary  $z$  rotations and have neglected the subdominant errors in the  $|\overline{00}\rangle$ ,  $|\overline{01}\rangle$ , and  $|\overline{10}\rangle$  channels. The population error has been written in terms of a rotation angle error  $\theta$ , which will be interpreted (see below) as the deviation from  $2\pi$  of the rotation angle in the two-dimensional subspace spanned by  $|11\rangle$  and  $|20\rangle$ . The expression (96) does not include switching errors because we are evaluating the effect of pulse-shape errors on an otherwise perfect, large- $\sigma$  CZ gate. The average fidelity loss  $\mathbb{E} \equiv 1 - F_{\text{ave}}$  associated with (96) is, to leading order,

$$\mathbb{E} = \frac{3}{20} \delta^2 + \frac{1}{16} \theta^2. \quad (97)$$

What remains is to express the controlled phase error  $\delta$  and rotation error angle  $\theta$  in terms of  $\delta t_{\text{on}}$  and  $\delta \omega_{\text{on}}$ . This involves only the two channels  $|\overline{11}\rangle$  and  $|\overline{20}\rangle$  of the qubit-resonator model (9), and we will use the same small- $\sigma$  approximation used in Sec. III B for our analysis of the  $|\overline{11}\rangle$  channel dynamics. In the  $\{|11\rangle, |20\rangle\}$  basis, (9) can be written as

$$H = \begin{pmatrix} \epsilon + \omega_b & \sqrt{2}g_b \\ \sqrt{2}g_b & 2\epsilon - \eta \end{pmatrix}. \quad (98)$$

The eigenstates of (98) are

$$|\overline{11}\rangle = \cos \frac{\zeta}{2} |11\rangle - \sin \frac{\zeta}{2} |20\rangle, \quad (99)$$

$$|\overline{20}\rangle = \cos \frac{\zeta}{2} |20\rangle + \sin \frac{\zeta}{2} |11\rangle, \quad (100)$$

where

$$\zeta \equiv \arctan \left( \frac{2\sqrt{2}g_b}{\epsilon - \omega_{\text{on}}} \right), \quad (101)$$

and the energies are

$$E_{11} = \epsilon + \omega_b + \frac{\epsilon - \omega_{\text{on}}}{2} - \sqrt{\left( \frac{\epsilon - \omega_{\text{on}}}{2} \right)^2 + (\sqrt{2}g_b)^2}, \quad (102)$$

$$E_{20} = \epsilon + \omega_b + \frac{\epsilon - \omega_{\text{on}}}{2} + \sqrt{\left(\frac{\epsilon - \omega_{\text{on}}}{2}\right)^2 + (\sqrt{2}g_b)^2}. \quad (103)$$

Here we have used the expression (11) for  $\omega_{\text{on}}$ , which is appropriate for the model (98).

The analysis below follows that of the  $|\overline{11}\rangle$  channel evolution given Sec. III B, except here we introduce a timing error  $\delta t_{\text{on}}$  and a tuning error  $\delta\omega_{\text{on}}$ . Starting in the strongly detuned configuration with  $\epsilon - \omega_{\text{on}} \gg g_b$  in the eigenstate  $|\overline{11}\rangle \approx |11\rangle$ , and quickly switching to  $\epsilon = \omega_{\text{on}} + \delta\omega_{\text{on}}$ , leaves the system in the state,

$$|11\rangle = \cos \frac{\zeta_{\text{on}}}{2} |\overline{11}\rangle + \sin \frac{\zeta_{\text{on}}}{2} |\overline{20}\rangle. \quad (104)$$

Here  $\zeta_{\text{on}} \equiv \arctan(2\sqrt{2}g_b/\delta\omega_{\text{on}})$ , and the eigenstates in (104) are for  $\epsilon = \omega_{\text{on}} + \delta\omega_{\text{on}}$ . Note that (104) reduces to (24) in the  $\delta\omega_{\text{on}} \rightarrow 0$  limit. Evolution with  $\epsilon$  fixed at  $\omega_{\text{on}} + \delta\omega_{\text{on}}$  for a time,

$$\frac{2\pi}{E_{20} - E_{11}} = \frac{\pi}{\sqrt{(\delta\omega_{\text{on}}/2)^2 + (\sqrt{2}g_b)^2}}, \quad (105)$$

would implement a  $2\pi$  rotation in the  $\{|11\rangle, |\overline{20}\rangle\}$  subspace, returning to  $|11\rangle$  with a phase shift that depends on  $\delta\omega_{\text{on}}$ . We intentionally introduce a  $t_{\text{on}}$  pulse shape error and instead evolve for a time,

$$t = \frac{\pi}{\sqrt{(\delta\omega_{\text{on}}/2)^2 + (\sqrt{2}g_b)^2}} + \delta t_{\text{on}}, \quad (106)$$

after which we detune and find the final state,

$$\begin{aligned} & -e^{i\delta} \cos \frac{\theta}{2} |11\rangle + \text{phase factor} \times \sqrt{\mathbb{E}_\theta} |\overline{20}\rangle \\ & \approx -e^{i\delta} \cos \frac{\theta}{2} |\overline{11}\rangle + \text{phase factor} \times \sqrt{\mathbb{E}_\theta} |\overline{20}\rangle, \end{aligned} \quad (107)$$

where

$$\delta = -\frac{\pi \delta\omega_{\text{on}}}{2\sqrt{2}g_b}, \quad (108)$$

and

$$\mathbb{E}_\theta \equiv \sin^2 \frac{\theta}{2} = 2g_b^2 \delta t_{\text{on}}^2. \quad (109)$$

These expressions are valid to leading order in  $\delta\omega_{\text{on}}$  or  $\delta t_{\text{on}}$ , neglecting cross terms. Here  $\mathbb{E}_\theta$  is the probability of leakage to  $|\overline{20}\rangle$  resulting from a  $t_{\text{on}}$  error, which, as discussed above, causes a rotation error of angle  $\theta$ . An alternative estimate for  $\theta$  (and hence  $\mathbb{E}_\theta$ ) is

$$\theta \approx \frac{\delta t_{\text{on}}}{t_{\text{on}}} \times 2\pi, \quad (110)$$

which also gives (109) [after using the sudden limit result (4) for  $t_{\text{on}}$ ]. Note that the leakage error  $\mathbb{E}_\theta$  is independent of  $\delta\omega_{\text{on}}$  (to this order), enabling the phase  $\delta$  to be intentionally adjusted by varying  $\omega_{\text{on}}$  only. Doing this generates (approximately)

TABLE III. CZ pulse shape precision requirements. The bounds listed in the  $t_{\text{on}}$  column assume that this is the only type of pulse parameter inaccuracy present, with an (estimated) error given in the first column, and that the auxiliary  $z$  rotation angles are reoptimized and implemented perfectly. The  $\omega_{\text{on}}$  bounds are defined analogously. The error  $\mathbb{E}$  is defined in (97).

$\mathbb{E}$	$t_{\text{on}}$ precision	$\omega_{\text{on}}$ precision
$10^{-3}$	160 ps	4 MHz
$10^{-4}$	50 ps	1 MHz

gates of the form,

$$\begin{pmatrix} 1 & 0 & 0 & 0 \\ 0 & 1 & 0 & 0 \\ 0 & 0 & 1 & 0 \\ 0 & 0 & 0 & e^{i(\pi+\delta)} \end{pmatrix}, \quad (111)$$

for small  $\delta$ , with alternative controlled phases [46]. Gates (approximately) of the form (111) with arbitrary—not necessarily small—values of  $\delta$  can be implemented by varying both  $\omega_{\text{on}}$  and  $t_{\text{on}}$  away from their optimal values.

Referring again to the 99.9% CZ gate of Table I designed for the  $\eta/2\pi = 300$  MHz transmon, we estimate from (97), (108), and (109) that a 10 ps error in  $t_{\text{on}}$  (or a 1 MHz error in  $\omega_{\text{on}}/2\pi$ ) with optimal  $z$  rotations would lead to a fidelity loss of about  $4.0 \times 10^{-6}$  (or  $9.1 \times 10^{-5}$ ), whereas numerical simulation of the same error in QVN<sub>4</sub>, which includes all subdominant processes, yields  $3.0 \times 10^{-6}$  (or  $1.1 \times 10^{-4}$ ).

Finally, it is interesting to use the above estimates to bound the magnitude of the allowable  $t_{\text{on}}$  and  $\omega_{\text{on}}$  errors, such that the resulting pulse shape errors (97) are subdominant to the  $10^{-3}$  or  $10^{-4}$  base gate error. This is done in Table III. For example, a 99.9% CZ gate from Table I with a  $t_{\text{on}}$  error of 160 ps will have an additional intrinsic error of  $10^{-3}$  (and a total error of about  $2 \times 10^{-3}$ ). Current experimental limitations on the control of  $t_{\text{on}}$  and  $\omega_{\text{on}}$  are considerably better than that required to suppress pulse shape errors below the  $10^{-4}$  level.

#### J. CZ gate with 99.999% fidelity

Higher fidelities are also possible with the pulse shape (1). An example is provided in Table IV for the 300 MHz qubit. For this design we did not perform a separate  $g_b$  optimization for this higher fidelity, but instead used the value from Table I optimized for the lower fidelities.

### IV. ADDITIONAL CZ GATES

#### A. CZ between bus and qubit $q_4$

The main focus of this paper is the CZ gate between qubit  $q_1$  and the bus in the QVN<sub>4</sub> processor. Results for the other

TABLE IV. Optimal QVN<sub>4</sub> gate fidelity for a Strauch CZ gate between qubit  $q_1$  and the bus.

$\eta/2\pi$	$g_b/2\pi$	$g_m/2\pi$	$t_{\text{ramp}}$	$\sigma$	$t_{\text{gate}}$	$F_{\text{ave}}$
300 MHz	45 MHz	100 MHz	13 ns	2.30 ns	25.7 ns	99.999%

qubits are very similar, with the worst case being  $q_4$ , because the detuning to memory during the gate is slightly smaller. We find that the intrinsic fidelity of the 99.9% CZ gate for the 300 MHz qubit given in Table I changes from 99.928% to 99.925% if qubit  $q_4$  is used instead of  $q_1$ .

### B. CZ between two qubits in QVN<sub>4</sub>

In this section we explain how to perform a CZ gate between two qubits—or more precisely, between two *memories*—in the QVN architecture. Such an operation is not elementary, as it can be composed of the qubit-bus CZ combined with MOVE gates. (There are also proposals for the direct implementation of a qubit-qubit CZ gate in a QVN device [47,59].) Figure 6 shows the experimental protocol for implementing the gate  $\text{cz}_{23}$  between qubits  $q_2$  and  $q_3$ , suppressing auxiliary  $z$  rotations, and with all data starting and ending in memory. This mode diagram shows the time dependence of all nine device frequencies. The color indicates whether the qubit or resonator would be in the ground state (blue or dark gray) or possibly excited state (red or light gray) in the weakly coupled limit. Modes are colored red if there is a finite occupation of the  $|1\rangle$  state (in the weakly coupled limit), for some choice of initial conditions. All qubits are initially parked at the strongly detuned frequency of 10 GHz. Horizontal lines 1–4 represent memories, and  $b$  is the bus. No red or red and blue lines with first-order *or* second-order couplings cross (to avoid Landau-Zener transitions), and no more than one qubit is occupied at any time (to avoid second-order qubit-qubit interactions mediated by the bus).

Beginning with the four memory registers in an arbitrary (possibly entangled) state, the bus is loaded by a 5 ns MOVE gate from  $m_3 \rightarrow q_3$  followed by a 10 ns MOVE to the bus. These are approximate gate times (time estimates for these gates are given in Sec. V and a concrete example is provided below). Qubit  $q_2$  is then loaded and tuned to the frequency  $\omega_{\text{on}}$  determined by optimization. This central portion of the gate is close (but not exactly the same as) the qubit-bus CZ gate of

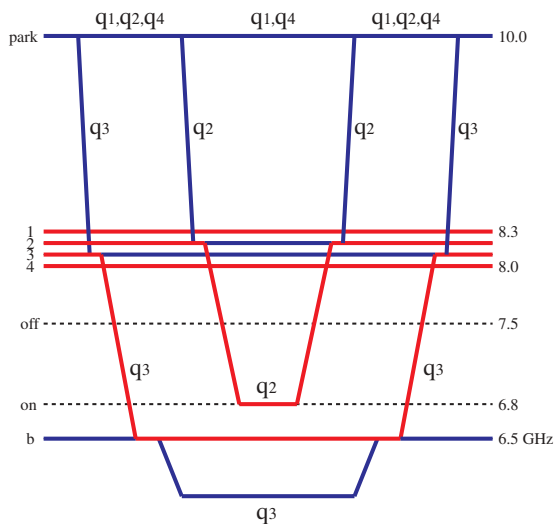


FIG. 6. (Color online) QVN<sub>4</sub> mode diagram for the  $\text{cz}_{23}$  gate. Gaussian filtering of the pulse is not shown.

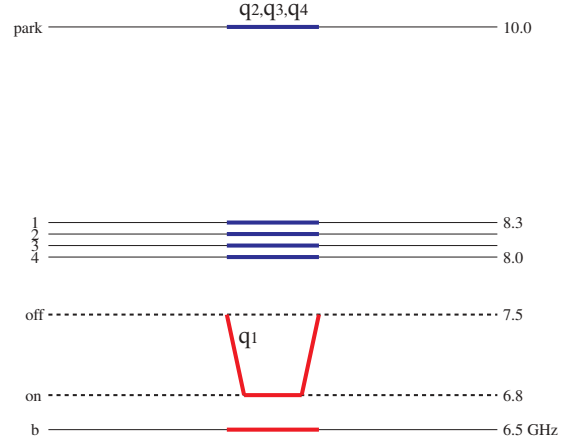


FIG. 7. (Color online) CZ gate between  $q_1$  and bus. This diagram describes the gate of Table I.

Table I, which, for the purposes of comparison, is shown in Fig. 7.

We simulated the gate  $\text{CZ}_{23}$  shown in Fig. 6, using the 99.99% CZ of Table I for a 300 MHz qubit, and starting with the memory register in the GHZ state,

$$\frac{|0000\rangle + |1111\rangle}{\sqrt{2}}. \quad (112)$$

The MOVE gates also have fidelities around 99.99%. Note that  $H_{\text{idle}}$  and the associated computational basis states (interacting eigenfunctions of  $H_{\text{idle}}$ ) are different at the beginning and end of each MOVE gate. The total  $\text{cz}_{23}$  gate time is

$$t_{\text{gate}} = 55 \text{ ns}, \quad (113)$$

and the final state fidelity (overlap squared) is

$$F = 99.94\%. \quad (114)$$

In addition to the 23 ns qubit-bus CZ gate, there are four MOVE to or from memory operations, each taking about 3.5 ns, and two MOVE to or from bus gates, each taking about 9 ns. There are also local  $z$  rotations (not shown) between each gate.

A few remarks about the encouraging result (114) are in order: The seven elementary gates making up the  $\text{CZ}_{23}$  operation are optimized individually to an error of about  $10^{-4}$ , and then combined without any additional optimization of the composite pulse sequence or control parameters, respecting the modularity required by scalable, gate-based quantum computation. And the total intrinsic error  $\mathbb{E} \equiv 1 - F = 6 \times 10^{-4}$  implied by (114) is consistent with a linear (incoherent) accumulation of errors with a number of elementary steps  $\mathbb{E}_{\text{inc}} \cong 7 \times 10^{-4}$ , but is not consistent with a quadratic (coherent) accumulation  $\mathbb{E}_{\text{coh}} \cong 7^2 \times 10^{-4}$ .

### C. Beyond QVN: CZ gate between directly coupled superconducting qubits

The main focus of this work is the CZ gate between a directly coupled qubit and resonator in a multiqubit QVN device. However, many of our results—especially the error analysis—will also be relevant for hardware designs incorporating pairs of directly coupled superconducting qubits, the system originally

considered by Strauch *et al.* [42]. Here we summarize the principal differences between the qubit-bus CZ gate of Sec. III and the directly coupled qubit-qubit gate. For the latter case we assume qubits with anharmonic detunings  $\eta_1$  and  $\eta_2$  [defined as in (7)] and a purely transverse (off-diagonal) capacitive coupling with interaction strength  $g$ .

The first difference concerns a *frequency asymmetry* of the qubit-bus gate. Recall from Sec. III B that the CZ gate is implemented by *decreasing* the qubit frequency  $\epsilon$  from a value far above  $\omega_b$  to (approximately)

$$\epsilon = \omega_b + \eta, \quad (115)$$

where  $\eta > 0$  is the qubit anharmonicity. By contrast, the qubit-qubit CZ gate can be implemented either by decreasing the frequency  $\epsilon_1$  of qubit 1 from a value far *above* that of a second qubit with a (fixed) frequency  $\epsilon_2$ , until

$$\epsilon_1 = \epsilon_2 + \eta_1, \quad (116)$$

which is directly analogous to (115), or from *below* by increasing to

$$\epsilon_1 = \epsilon_2 - \eta_2. \quad (117)$$

The conditions (116) and (117) specify the crossings of the bare  $|11\rangle$  state with  $|20\rangle$  and  $|02\rangle$ , respectively (in the basis  $|q_1 q_2\rangle$ ). The frequency asymmetry of the qubit-bus gate is a consequence of the harmonic spectrum of the bus and can be understood from Fig. 3, which shows that when  $|11\rangle$  reaches the  $|02\rangle$  crossing from below,  $|01\rangle$  and  $|10\rangle$  also become degenerate [as expected from (117) when  $\eta_2 \rightarrow 0$ ]. This would result in unwanted phase shifts of the  $|01\rangle$  and  $|10\rangle$  channels, as well as large switching errors between them.

The second major difference between the qubit-bus and qubit-qubit gates is that the additional anharmonicity in the latter case further suppresses the nonadiabatic switching errors and leads to better gate performance. This can be understood from the analysis of Sec. III H, noting that in the qubit-qubit case, adiabaticity of the  $|11\rangle$  channel is protected by an energy gap of size  $\eta_1 + \eta_2 - \sqrt{2}g$ , where  $g$  is the qubit-qubit interaction strength. Let's estimate the  $|11\rangle \rightarrow |02\rangle$  switching error  $\mathbb{E}_2$  for a qubit-qubit CZ gate at the upper frequency (116), with  $\eta_1 = \eta_2 = 2\pi \times 300$  MHz,  $g = 2\pi \times 45$  MHz, and  $t_{\text{ramp}} = 7$  ns. In this application we use formula (76) with parameter values,

$$G = \sqrt{2}g, \quad (118)$$

$$\Delta_{\text{on}} = \eta_1 + \eta_2 - \sqrt{2}g, \quad (119)$$

$$\Delta_{\text{off}} = 2\pi \times 1 \text{ GHz}. \quad (120)$$

We note from (119) that the anharmonicity suppressing the  $|11\rangle \rightarrow |02\rangle$  switching error is effectively doubled in the qubit-qubit system. With these parameters we obtain  $|A|^2 = 5.8 \times 10^{-6}$  and  $p_{\text{sw}} = 8.2 \times 10^{-8}$ .

Although the  $|11\rangle \rightarrow |02\rangle$  switching error is greatly reduced in the qubit-qubit CZ gate, the actual gate fidelity does not fully benefit from this reduction. This is because the dominant intrinsic error in the qubit-qubit gate is the switching error  $\mathbb{E}_1$  between  $|01\rangle$  and  $|10\rangle$ , or the reverse, which is subdominant in the qubit-bus case (see Sec. III H). In fact, the  $|01\rangle \leftrightarrow |10\rangle$  switching error estimate (87) also applies

to the qubit-qubit system (with  $\eta_1 = \eta_2 = 2\pi \times 300$  MHz,  $g = 2\pi \times 45$  MHz, and  $t_{\text{ramp}} = 7$  ns), resulting in an estimated minimum fidelity of

$$F_{\text{min}}^{(\text{est})} \equiv 1 - \mathbb{E}_1 = 1 - 2p_{\text{sw}} = 99.991\%. \quad (121)$$

## V. SYSTEM OPTIMIZATION

In this section we discuss an approach for choosing optimal QVN<sub>n</sub> device parameters. This is a complex global optimization problem that we will solve in a simple but approximate way, emphasizing the main ideas of the procedure instead of its most precise implementation.

First we consider resonator frequencies. The QVN<sub>n</sub> processor includes  $n$  memory resonators, with frequencies  $\omega_{m1}, \omega_{m2}, \dots$ . These need to be mutually detuned (to lift degeneracies), and for simplicity we space them by 100 MHz (a smaller value could be used). The band of memory frequencies itself needs to be well detuned from the bus to keep the idle error (to be discussed below) in check.

Because the qubit frequency during a qubit-bus CZ gate must approach the bus frequency from above (Sec. IV C), the bus frequency must be below the memory band. The choice of bus frequency therefore determines the lowest transition frequency that needs to be accessible by a qubit. Specifically, the qubits will need to tune 500 MHz or so below the bus (see Fig. 6). However, the minimum transition frequency may be constrained by qubit design (in addition to other considerations). In the tunable- $E_J$  transmon, for example, this minimum frequency depends on the qubit anharmonicity  $\eta$ . Here we will choose a minimum qubit frequency and corresponding bus frequency appropriate for a 300 MHz transmon. This leads to our choice of 6.5 GHz for the bus frequency. Optimal resonator frequencies for smaller  $\eta$  are unchanged, whereas for larger  $\eta$  they need to be rigidly shifted upward in frequency. In particular, system frequencies for a 400 MHz transmon will be shifted upward in frequency by about 2 GHz. Apart from this large but simple change, we expect the system optimization results, such as  $g_b$  values, to be valid for the 400 MHz case as well.

The frequency  $\omega_{\text{off}}$  can be viewed as defining a boundary between MOVE and CZ gates, or between consecutive MOVE gates (see Fig. 6, for example). It is also natural to perform single-qubit operations with microwave pulses at the qubit frequency  $\omega_{\text{off}}$ . If  $\omega_{\text{off}}$  is too low, the error of the (approximate two-parameter) MOVE to or from memory gate becomes significant (this is determined by the qubit-bus detuning because the dominant error is nonadiabatic leakage to the bus), whereas if  $\omega_{\text{off}}$  is too high the fidelity of the qubit-bus CZ degrades (because  $d\epsilon/dt$  increases). We find that 7.5 GHz works well. At least 500 MHz is required between  $\omega_{\text{off}}/2\pi$  and the memory band to keep the MOVE errors (to or from the bus) under control. Thus we arrive at the memory frequencies given in Table II.

Having obtained prospective resonator frequencies, we turn to couplings. The most frequently used gate is expected to be the MOVE to or from memory, which must be as fast as possible. Figure 6 includes four examples. The gate time for



this operation is, approximately,

$$\frac{\pi}{2g_m} + t_{\text{ramp}} + 1 \text{ ns}. \quad (122)$$

The first term is the  $\pi$  rotation time, and the second and third are switching times (the detuning ramp can be fast because the qubit is unoccupied). Choosing  $g_m/2\pi = 100$  MHz makes the first term 2.5 ns. It might be possible to increase  $g_m$  further, but suppressing the resulting idling error (see below) would require an even higher empty-qubit parking frequency. The value of  $t_{\text{ramp}}$  is determined by the desired MOVE gate fidelity. Because the dominant error is nonadiabatic excitation of the bus, we can estimate it using our expression (76) for the switching error  $p_{\text{sw}}$ , with  $G = g_b$ ,  $\Delta_{\text{on}}/2\pi = 1.0$  GHz, and  $\Delta_{\text{off}}/2\pi = 1.8$  GHz (corresponding to  $m_4$ , the worst case). These values depend on our initial resonator frequency assignments. From Fig. 5 we obtain  $|A|^2 = 0.03$  ( $9.8 \times 10^{-4}$ ) for a 1 ns (2 ns) ramp. Considering the largest (worst case) value for  $g_b/2\pi$  of 60 MHz gives  $p_{\text{sw}} = 1.1 \times 10^{-4}$  ( $3.5 \times 10^{-6}$ ) for a 1 ns (2 ns) ramp. Thus we conclude that the MOVE to or from memory can be done in about 5 ns if  $g_m/2\pi = 100$  MHz. (Here we assumed the simplest 2 + 1-parameter MOVE to or from memory gate, having two pulse-shape parameters and one auxiliary  $z$  rotation angle. It is also possible to implement this gate with even higher fidelity with 4 + 1 parameters [34].)

The bus coupling is found by the following “ $g$ -optimization” procedure: Consider the set of discretized  $g_b/2\pi$  values, varying from 10 to 100 MHz in steps of 1 MHz. For each value of  $g_b$ , calculate the minimum value of  $t_{\text{ramp}}$  and the associated  $t_{\text{gate}}$  required to achieve a target fidelity, say 99.9%. We do this by stepping through  $t_{\text{ramp}}$  values, estimating the fidelity using (76) and (84) from Sec. III H, which is very efficient, then confirming through a full optimization on QVN<sub>1</sub>. We then obtain, for each  $g_b$ , the gate time of a 99.9% CZ gate, or equivalently, the function,

$$t_{\text{gate}}^{(99.9\%)}(g_b). \quad (123)$$

The function (123) gives the time required for a CZ gate with a given target fidelity as a function of  $g_b$ . Strict  $g$  optimization requires choosing  $g_b$  to minimize  $t_{\text{gate}}$ , and this procedure leads to the best performance in any given situation. However, carrying this out leads to a different  $g_b$  for each target fidelity. Fortunately, the curvature at the minimum in (123) is small and the simpler  $g_b$  values reported in Table I, which are independent of the target fidelity and are also constrained to be multiples of 5 MHz, lead to very little performance loss, typically 1–2 ns in gate time.

Having obtained prospective resonator frequencies and couplings, we choose the empty qubit parking frequency  $\omega_{\text{park}}$  to control the idle error,

$$\mathbb{E} = (\Omega_{ZZ}t)^2 n^2, \quad (124)$$

where  $\Omega_{ZZ}$  is the effective  $\sigma^z \otimes \sigma^z$  coupling frequency between a memory resonator and the bus, induced by their shared qubit [34]. The  $n$  dependence in (124) assumes the worst case. Assuming  $\omega_{\text{park}}/2\pi = 10$  GHz,  $g_b/2\pi = 60$  MHz (the worst case), and  $\eta/2\pi = 400$  MHz (also the worst case) leads to

$$\frac{\Omega_{ZZ}}{2\pi} = -0.881 \text{ kHz}. \quad (125)$$

It will be necessary to keep (124) less than the fault-tolerant threshold during a (potentially) long error correction cycle. If we assume  $t = 1 \mu\text{s}$ , the idle error in QVN<sub>4</sub> is  $4.9 \times 10^{-4}$ , which is acceptable. Reducing the parked qubit frequency to 9.5 GHz (9.0 GHz) increases the idle error to  $3.8 \times 10^{-3}$  ( $7.3 \times 10^{-2}$ ).

We are now able to calculate the gate time of the MOVE to or from bus operation. The gate time is, approximately,

$$\frac{\pi}{2g_b} + t_{\text{ramp}} + 1 \text{ ns}, \quad (126)$$

where the first term is between 4 and 8 ns for the bus couplings in Table I. As before,  $t_{\text{ramp}}$  is determined by the desired gate fidelity. The dominant error is nonadiabatic transition to memory, which we estimate using (76) with  $G = g_m$ ,  $\Delta_{\text{on}}/2\pi = 0.5$  GHz (the worst case), and  $\Delta_{\text{off}}/2\pi = 1.5$  GHz. Note that this error is enhanced by the large value of  $g_m$ . From Fig. 5 we obtain  $|A|^2 = 5.9 \times 10^{-2}$  ( $1.6 \times 10^{-2}$ ) for a 2 ns (3 ns) ramp. Then  $p_{\text{sw}} = 2.4 \times 10^{-4}$  ( $6.4 \times 10^{-4}$ ) for a 2 ns (3 ns) ramp. Thus we conclude that the MOVE to or from bus takes between 7 and 12 ns, depending on the actual value of  $g_b$  and on the desired fidelity.

Finally, we confirm that the assumed qubit parameters are compatible with transmons. In the large  $E_J/E_C$  transmon regime, the qubit frequency  $\epsilon$  and anharmonicity  $\eta$  are given by [4]

$$\epsilon = \sqrt{8E_J E_C} - E_C, \quad (127)$$

and

$$\eta = E_C. \quad (128)$$

We assume a split-junction flux-biased Cooper-pair box so that  $E_J$  is tunable [43]. (Note that the tunable- $E_J$  transmon is sensitive to flux noise, which will degrade  $T_2$ .) Combining (127) and (128) leads to the relation  $\epsilon = \eta(\sqrt{8E_J/E_C} - 1)$  plotted in Fig. 8 for 300 and 400 MHz anharmonicity. Because  $E_J/E_C$  needs to be above about 50 to effectively suppress charge noise, we see that the 300 MHz transmon can have a transition frequency as small as 5.5 GHz, whereas the 400 MHz transmon has a minimum frequency of about

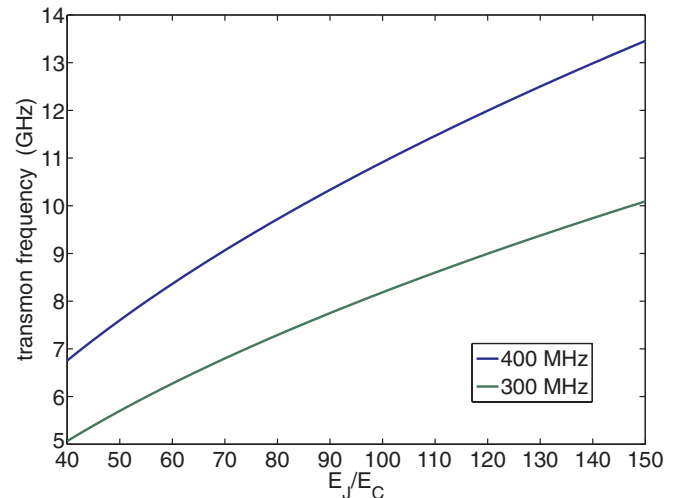


FIG. 8. (Color online) Transition frequency for transmon with 300 and 400 MHz anharmonicity.

7.5 GHz. Our choice of bus frequency is indeed consistent with the 300 MHz transmon, whereas  $\omega_b/2\pi$  and the entire spectrum of device frequencies would have to be increased by about 2 GHz for the 400 MHz transmon.

## VI. CONCLUSIONS

We have investigated the problem of CZ gate design for the superconducting QVN architecture based on a realistic, two-parameter filtered rectangular pulse (1). The gate operates by using the noncomputational qubit  $|2\rangle$  state as first proposed by Strauch *et al.* [42]. The main results are summarized in Table I. The use of interacting eigenfunctions as computational basis states, and the use of auxiliary  $z$  rotations on the qubits and bus are critical to obtaining this high performance. The ability to perform SU(2) operations on the bus resonator is nontrivial because they cannot be implemented directly with microwave pulses or frequency excursions; instead, they must be compiled into future qubit rotations.

Our investigation is limited to and constrained by the pulse profile (1). Fidelity optimization determines the amount of time to spend switching the qubit and how long to stay at the “on” frequency. We find that this pulse shape correctly captures the relevant pulse degrees of freedom for fidelities up to about 99.99%. For higher fidelity gates, which are slower and which would require larger coupling, alternative few-parameter pulse shapes where most of the time is spent switching, could become competitive with (1). Although we are able to obtain fidelities well above 99.99% with profile (1),

it is possible that alternative few-parameter pulse shapes would be able to achieve the same intrinsic fidelity in less gate time.

One can also consider more complex pulse shapes with many control parameters, which can achieve nearly perfect intrinsic fidelity in a time  $t_{\text{gate}}$  (depending on  $g_b$ ) significantly shorter than obtained with pulse shape (1). Egger *et al.* [59] have recently investigated this optimal control approach (using the gradient pulse shape engineering method of Khaneja *et al.* [60]), and have obtained about a factor of two speedup for a qubit-qubit CZ gate similar to that of Sec. IV B. This approach clearly warrants further investigation and experimental implementation.

We did not include the effects of decoherence (or flux noise) in this work. However, an order-of-magnitude estimate of the  $T_1$  decay error  $\mathbb{E} \approx t_{\text{gate}}/T_1$  suggests that it should be possible to demonstrate a 99.9% CZ gate with existing transmon qubits, which would be an important step towards the development of fault-tolerant quantum computation.

*Note added in proof.* We would like to bring attention to Ref. [61], which is also relevant to this work.

## ACKNOWLEDGMENTS

This work was supported by the Intelligence Advanced Research Projects Activity under Army Research Office Grant No. W911NF-10-1-0334. It is a pleasure to thank Leonardo DiCarlo, Matteo Mariantoni, and Frank Wilhelm for useful discussions.

- 
- [1] J. Q. You and F. Nori, in *Superconducting Circuits and Quantum Information*, Physics Today, November (American Institute of Physics, Melville, 2005), p. 42.
  - [2] R. J. Schoelkopf and S. M. Girvin, *Nature (London)* **451**, 664 (2008).
  - [3] J. Clarke and F. K. Wilhelm, *Nature (London)* **453**, 1031 (2008).
  - [4] J. Koch, T. M. Yu, J. Gambetta, A. A. Houck, D. I. Schuster, J. Majer, A. Blais, M. H. Devoret, S. M. Girvin, and R. J. Schoelkopf, *Phys. Rev. A* **76**, 042319 (2007).
  - [5] A. A. Houck, J. Koch, M. H. Devoret, S. M. Girvin, and R. J. Schoelkopf, *Quantum Inf. Proc.* **8**, 105 (2009).
  - [6] H. Paik, D. I. Schuster, L. S. Bishop, G. Kirchmair, G. Catelani, A. P. Sears, B. R. Johnson, M. J. Reagor, L. Frunzio, L. I. Glazman, S. M. Girvin, M. H. Devoret, and R. J. Schoelkopf, *Phys. Rev. Lett.* **107**, 240501 (2011).
  - [7] C. Rigetti, J. M. Gambetta, S. Poletto, B. L. T. Plourde, J. M. Chow, A. D. Corcoles, J. A. Smolin, S. T. Merkel, J. R. Rozen, G. A. Keefe, M. B. Rothwell, M. B. Ketchen, and M. Steffen, *Phys. Rev. B* **86**, 100506 (2012).
  - [8] F. Mallet, F. R. Ong, A. Palacios-Laloy, F. Nguyen, P. Bertet, D. Vion, and D. Esteve, *Nat. Phys.* **5**, 791 (2009).
  - [9] B. R. Johnson, M. D. Reed, A. A. Houck, D. I. Schuster, L. S. Bishop, E. Ginossar, J. M. Gambetta, L. DiCarlo, L. Frunzio, S. M. Girvin, and R. J. Schoelkopf, *Nat. Phys.* **6**, 663 (2010).
  - [10] M. Boissonneault, J. M. Gambetta, and A. Blais, *Phys. Rev. Lett.* **105**, 100504 (2010).
  - [11] M. D. Reed, L. DiCarlo, B. R. Johnson, L. Sun, D. I. Schuster, L. Frunzio, and R. J. Schoelkopf, *Phys. Rev. Lett.* **105**, 173601 (2010).
  - [12] J. E. Johnson, C. Macklin, D. H. Slichter, R. Vijay, E. B. Weingarten, J. Clarke, and I. Siddiqi, *Phys. Rev. Lett.* **109**, 050506 (2012).
  - [13] T. Hime, P. A. Reichardt, B. L. T. Plourde, T. L. Robertson, C.-E. Wu, V. A. Ustinov, and J. Clarke, *Science* **314**, 1427 (2006).
  - [14] S. H. W. van der Ploeg, A. Izmalkov, A. M. van den Brink, U. Hubner, M. Grajcar, E. Il'ichev, H.-G. Meyer, and A. M. Zagorskin, *Phys. Rev. Lett.* **98**, 057004 (2007).
  - [15] A. O. Niskanen, K. Harrabi, F. Yoshihara, Y. Nakamura, S. Lloyd, and J. S. Tsai, *Science* **316**, 723 (2007).
  - [16] R. Harris, A. J. Berkley, M. W. Johnson, P. Bunyk, S. Govorkov, M. C. Thom, S. Uchaikin, A. B. Wilson, J. Chung, E. Holtham, J. D. Biamonte, A. Y. Smirnov, M. H. S. Amin, and A. Maassen van den Brink, *Phys. Rev. Lett.* **98**, 177001 (2007).
  - [17] M. S. Allman, F. Altomare, J. D. Whittaker, K. Cicak, D. Li, A. Sirois, J. Strong, J. D. Teufel, and R. W. Simmonds, *Phys. Rev. Lett.* **104**, 177004 (2010).
  - [18] R. C. Bialczak, M. Ansmann, M. Hofheinz, M. Lenander, E. Lucero, M. Neeley, A. D. O'Connell, D. Sank, H. Wang, M. Weides, J. Wenner, T. Yamamoto, A. N. Cleland, and J. M. Martinis, *Phys. Rev. Lett.* **106**, 060501 (2011).
  - [19] P. Groszkowski, A. G. Fowler, F. Motzoi, and F. K. Wilhelm, *Phys. Rev. B* **84**, 144516 (2011).

- [20] J. Q. You, Y. Nakamura, and F. Nori, *Phys. Rev. B* **71**, 024532 (2005).
- [21] C. Rigetti, A. Blais, and M. H. Devoret, *Phys. Rev. Lett.* **94**, 240502 (2005).
- [22] Y.-X. Liu, L. F. Wei, J. S. Tsai, and F. Nori, *Phys. Rev. Lett.* **96**, 067003 (2006).
- [23] G. S. Paraoanu, *Phys. Rev. B* **74**, 140504 (2006).
- [24] S. Ashhab, S. Matsuo, N. Hatakenaka, and F. Nori, *Phys. Rev. B* **74**, 184504 (2006).
- [25] M. Grajcar, Y.-X. Liu, F. Nori, and A. M. Zagorskin, *Phys. Rev. B* **74**, 172505 (2006).
- [26] S. Ashhab and F. Nori, *Phys. Rev. B* **76**, 132513 (2007).
- [27] Y.-X. Liu, L. F. Wei, J. R. Johansson, J. S. Tsai, and F. Nori, *Phys. Rev. B* **76**, 144518 (2007).
- [28] C. Rigetti and M. Devoret, *Phys. Rev. B* **81**, 134507 (2010).
- [29] P. C. de Groot, J. Lisenfeld, R. N. Schouten, S. Ashhab, A. Lupascu, C. J. P. M. Harmans, and J. E. Mooij, *Nat. Phys.* **6**, 763 (2010).
- [30] J. M. Chow, A. D. Corcoles, J. M. Gambetta, C. Rigetti, B. R. Johnson, J. A. Smolin, J. R. Rozen, G. A. Keefe, M. B. Rothwell, M. B. Ketchen, and M. Steffen, *Phys. Rev. Lett.* **107**, 080502 (2011).
- [31] P. C. de Groot, S. Ashhab, A. Lupascu, L. DiCarlo, F. Nori, C. J. P. M. Harmans, and J. E. Mooij, *New J. Phys.* **14**, 073038 (2012).
- [32] J. M. Chow, J. M. Gambetta, A. D. Corcoles, S. T. Merkel, J. A. Smolin, C. Rigetti, S. Poletto, G. A. Keefe, M. B. Rothwell, J. R. Rozen, M. B. Ketchen, and M. Steffen, *Phys. Rev. Lett.* **109**, 060501 (2012).
- [33] M. Mariantoni, H. Wang, T. Yamamoto, M. Neeley, R. C. Bialczak, Y. Chen, M. Lenander, E. Lucero, A. D. O'Connell, D. Sank, M. Weides, J. Wenner, Y. Yin, J. Zhao, A. N. Korotkov, A. N. Cleland, and J. M. Martinis, *Science* **334**, 61 (2011).
- [34] A. Galiatdinov, A. N. Korotkov, and J. M. Martinis, *Phys. Rev. A* **85**, 042321 (2012).
- [35] J. M. Martinis, *Quantum Inf. Proc.* **8**, 81 (2009).
- [36] D. P. DiVincenzo, *Phys. Scr., T* **137**, 014020 (2009).
- [37] J. Ghosh, A. G. Fowler, and M. R. Geller, *Phys. Rev. A* **86**, 062318 (2012).
- [38] F. Motzoi, J. M. Gambetta, P. Rebentrost, and F. K. Wilhelm, *Phys. Rev. Lett.* **103**, 110501 (2009).
- [39] J. M. Gambetta, F. Motzoi, S. T. Merkel, and F. K. Wilhelm, *Phys. Rev. A* **83**, 012308 (2011).
- [40] M. Hofheinz, E. M. Weig, M. Ansmann, R. C. Bialczak, E. Lucero, M. Neeley, A. D. O'Connell, H. Wang, J. M. Martinis, and A. N. Cleland, *Nature (London)* **454**, 310 (2008).
- [41] M. Hofheinz, H. Wang, M. Ansmann, R. C. Bialczak, E. Lucero, M. Neeley, A. D. O'Connell, J. Sank, D. Wenner, J. M. Martinis, and A. N. Cleland, *Nature (London)* **459**, 546 (2009).
- [42] F. W. Strauch, P. R. Johnson, A. J. Dragt, C. J. Lobb, J. R. Anderson, and F. C. Wellstood, *Phys. Rev. Lett.* **91**, 167005 (2003).
- [43] L. DiCarlo, J. M. Chow, J. M. Gambetta, L. S. Bishop, D. I. Schuster, J. Majer, A. Blais, L. Frunzio, S. M. Girvin, and R. J. Schoelkopf, *Nature (London)* **460**, 240 (2009).
- [44] G. Haack, F. Helmer, M. Mariantoni, F. Marquardt, and E. Solano, *Phys. Rev. B* **82**, 024514 (2010).
- [45] L. DiCarlo, M. D. Reed, L. Sun, B. R. Johnson, J. M. Chow, J. M. Gambetta, L. Frunzio, S. M. Girvin, M. H. Devoret, and R. J. Schoelkopf, *Nature (London)* **467**, 574 (2010).
- [46] T. Yamamoto, M. Neeley, E. Lucero, R. C. Bialczak, J. Kelly, M. Lenander, M. Mariantoni, A. D. O'Connell, D. Sank, H. Wang, M. Weides, J. Wenner, Y. Yin, A. N. Cleland, and J. M. Martinis, *Phys. Rev. B* **82**, 184515 (2010).
- [47] A. Galiatdinov, arXiv:1103.4641.
- [48] X.-Y. Lu, S. Ashhab, W. Cui, R. Wu, and F. Nori, *New J. Phys.* **14**, 073041 (2012).
- [49] S. B. Bravyi and A. Y. Kitaev, arXiv:quant-ph/9811052.
- [50] R. Raussendorf and J. Harrington, *Phys. Rev. Lett.* **98**, 190504 (2007).
- [51] A. G. Fowler, A. M. Stephens, and P. Groszkowski, *Phys. Rev. A* **80**, 052312 (2009).
- [52] P. R. Johnson, F. W. Strauch, A. J. Dragt, R. C. Ramos, C. J. Lobb, J. R. Anderson, and F. C. Wellstood, *Phys. Rev. B* **67**, 020509 (2003).
- [53] A. Blais, A. Maassen van den Brink, and A. M. Zagorskin, *Phys. Rev. Lett.* **90**, 127901 (2003).
- [54] L. Pryadko and A. Korotkov (unpublished).
- [55] D. P. DiVincenzo, arXiv:quant-ph/0002077.
- [56] L. Viola and S. Lloyd, *Phys. Rev. A* **58**, 2733 (1998).
- [57] P. Zanardi and D. A. Lidar, *Phys. Rev. A* **70**, 012315 (2004).
- [58] L. H. Pedersen, N. M. Moller, and K. Molmer, *Phys. Lett. A* **367**, 47 (2007).
- [59] D. Egger, S. T. Merkel, and F. K. Wilhelm (unpublished).
- [60] N. Khaneja, T. Reiss, C. Kehlet, T. Schulte-Herbruggen, and S. J. Glaser, *J. Magn. Reson.* **172**, 296 (2005).
- [61] S. Ashhab, P. C. de Groot, and F. Nori, *Phys. Rev. A* **85**, 052327 (2012).